Final Technical Report (FTR) Instructions

Solar Energy Technologies Office (August 2023)

Final Technical Report (FTR)

Cover Page

a. *Federal Agency*	Department of Energy	
b. *Award Number*	DE-EE0009377	
c. *Project Title*	Enhancing particle-to-sCO_2 heat exchanger effectiveness through novel high-porosity metallic foams	
d. *Recipient Organization*	Mississippi State University	
e. *Project Period*	*Start:* 3/1/2021	*End:* 10/10/2024
f. *Principal Investigator (PI)*	Name: Prashant Singh, Ph.D. Title: Assistant Professor Email address: psingh15@utk.edu Phone number: 865-974-8994	
g. *Business Contact (BC)*	Name: Anna-Marie Nickels Title: Interim Manager, Sponsored Programs Accountant Email address: anickels@controller.msstate.edu Phone number: 662-338-6802	
h. *Certifying Official (if different from the PI or BC)*	Name: Prashant Singh, Ph.D. Title: Assistant Professor Email address: psingh15@utk.edu Phone number: 865-974-8994	

Prashant Singh — *11/8/24*

Signature of Certifying Official — *Date*

By signing this report, I certify to the best of my knowledge and belief that the report is true, complete, and accurate. I am aware that any false, fictitious, or fraudulent information, misrepresentations, half-truths, or the omission of any material fact, may subject me to criminal, civil or administrative penalties for fraud, false statements, false claims or otherwise. (U.S. Code Title 18, Section 1001, Section 287 and Title 31, Sections 3729-3730). I further understand and agree that the information contained in this report are material to Federal agency's funding decisions and I have any ongoing responsibility to promptly update the report within the time frames stated in the terms and conditions of the above referenced Award, to ensure that my responses remain accurate and complete.

1. **Acknowledgement:** "This material is based upon work supported by the U.S. Department of Energy's Office of Energy Efficiency and Renewable Energy (EERE) Solar Energy Technologies Office (SETO) under the DE-FOA-0002243 award number DE-EE0009377."

2. **Disclaimer**: “This report was prepared as an account of work sponsored by an agency of the United States Government. Neither the United States Government nor any agency thereof, nor any of their employees, makes any warranty, express or implied, or assumes any legal liability or responsibility for the accuracy, completeness, or usefulness of any information, apparatus, product, or process disclosed, or represents that its use would not infringe privately owned rights. Reference herein to any specific commercial product, process, or service by trade name, trademark, manufacturer, or otherwise does not necessarily constitute or imply its endorsement, recommendation, or favoring by the United States Government or any agency thereof. The views and opinions of authors expressed herein do not necessarily state or reflect those of the United States Government or any agency thereof.”

3. Executive Summary:

In this project, a novel concept of Octet-shape based lattice frame material was developed for deployment in particle-to-sCO_2 heat exchangers for CSP application. A comprehensive experimental and numerical program was performed to investigate and characterize the thermal and flow transport behavior in high porosity lattice frame material. The thermal properties include effective thermal conductivity and interstitial heat transfer coefficient and flow properties including permeability and inertial coefficient. Above quantities were determined for both air flow and heated particle flow through the porous channels which were representative of the hot channel in a typical counter flow heat exchanger. The cold side of the heat exchanger feature minichannels which are known to be very efficient in thermal transport. The goal of this project was to enhance the overall heat transfer coefficient (U_p) on the hot side by introducing Octet-shape based lattice frame material through enhancement in effective thermal conductivity of the channel and through enhancement in the interstitial heat transfer coefficient by the virtue of the particle interaction and the fibers. Through the validated computational model, a wide range of geometrical parameters were simulated for identification of optimized topology on the hot side. This exercise was followed by additive manufacturing of selected configurations (which allow particle flow) and subsequent integration with parallel plate assemblies featuring minichannels (which support sCO2 flow) obtained through diffusion bonding of chemically etched plates together. Comprehensive experimental program was executed to determine the convective heat transfer coefficient for wide range of particle flow rates and particle types in a moving packed bed orientation. A dedicated particle elevator and heat exchanger test facility was constructed to achieve the project goals and objectives. The parallel plates featured series of interconnected Octet-shaped lattice structures, which resulted in 40% enhancement in convective heat transfer compared to the baseline case of parallel plates alone. Discrete element modeling (DEM) studies were also conducted to understand the particle flowability through the complex lattice channels. A robust experimentally validated DEM study revealed that particle velocities increase when they move around the struts, which resulted in increased heat transfer. Further, the presence of struts also resulted in the creation of void and dead zones for particles.

The findings from the experimental, computational and analytical studies were used to design a particle-to-sCO2 heat exchanger for testing at the Sandia test bench. The heat exchanger was fabricated by assembling additively manufactured Octet lattice coupons with chemically etched minichannel plates. The experiments were conducted at a wide range of particle and sCO2 mass flow rates, while also varying the inlet temperature conditions. This project successfully demonstrated the promise of incorporating additively manufactured concepts for fabrication of compact and high-performance heat exchangers, which would significantly help in the reduction in levelized cost of electricity through utilizing concentrated solar thermal energy.

4. Table of Contents:

5. Background:

The renewable energy sources, including wind, solar, hydro, and geothermal, have been extensively investigated in many geographical areas worldwide. According to International Energy Agency (IEA), the contribution of renewable energy sources to worldwide electricity generation is rapidly increasing with 38% share recorded in 2022 [1]. Solar energy has become the predominant form of clean energy due to its widespread availability throughout the year. According to the IEA, solar energy accounted for 10.3% of worldwide electricity output in 2022. It is expected that solar energy would have the most substantial growth in the foreseeable future, mostly attributed to the ongoing reduction in the cost of solar energy-based power generation. According to IEA, there is a projected increase in global solar capacity from 843 gigawatts (GW) in 2022 to 2,800 GW by 2030 [2]. It is projected that the solar market in the United States would experience a threefold increase in size by the year 2028, resulting in the installation of approximately 375 GW of solar power [3,4]. As of now, solar photovoltaic (PV) stands as the most economically viable technology and is a prevalent method for harnessing solar energy. CSP is anticipated to have a substantial impact, particularly in large-scale solar initiatives. Concentrating Solar Power (CSP) plants have the capability to offer dependable and dispatchable electricity, which is of utmost importance in ensuring the stability of the power grid. Furthermore, CSP technology exhibits an advantage over PV due to its ability to facilitate thermal energy storage (TES), whereas PV technology involves the use of costly batteries.

The predominant form of TES technology employed in CSP facilities is based on molten salts. This system effectively stores thermal energy by utilizing a mixture of sodium nitrate and potassium nitrate in a molten state. Molten salts have the capability to attain elevated temperatures, reaching up to 565°C. This characteristic enables molten salt TES systems to store large amounts of energy and generate electricity over prolonged

durations, including during the absence of solar radiation. Some examples of current CSP power storage projects include the Andasol Solar Power Facility in Spain, the Crescent Dunes Solar Power Plant in Nevada USA, and the Noor Energy Complex in Morocco, which have molten salt TES systems capable of storing enough energy to generate electricity for 7.5, 10, and 7 hours without sunlight, respectively [5]. Despite being extensively utilized in modern CSP facilities, the implementation of molten salt encounters various obstacles, including its high cost [6], corrosive effects on CSP components [7], and the possibility of system malfunctions arising from salt solidification [8]. Furthermore, the existing molten salt technique is based on a binary composition including 60% sodium nitrate ($NaNO_3$) and 40% potassium nitrate (KNO_3), which exhibits a tendency to deteriorate when subjected to temperatures over 565°C [9]. These issues inhibit the employment of molten salt-based solutions in operational environments with temperatures exceeding 700°C- a critical need to advance the levelized cost of electricity targets for solar-based power generation. Higher operating temperatures augment power generation efficiency by improving the thermodynamic efficiency of the power cycle.

The ongoing development of next generation CSP facilities, also referred to as Gen3 CSP plants in the U.S., aims to enhance the efficiency, cost-effectiveness, and reliability of CSP technology. Gen3 CSP plants in the U.S. aim to operate at elevated temperatures [10], have alternative heat transfer fluids such as more thermally stable molten salts [11] and utilize supercritical fluids (SCFs), advanced solar collectors, and innovative thermal energy storage devices [12]. Gen3 CSP was launched by the U.S. Department of Energy (DOE) in 2017 with the primary objective to achieve a significant reduction in the cost of energy generated by CSP below $0.05 per kilowatt-hour (kWh) by 2030 [13]. The Gen3-CSP plants will be required to operate at temperatures over 700°C [14], leading to enhanced efficiency in electricity generation. The operation at elevated temperatures enables the exploitation of power cycles that are considerably more efficient, employing alternative working fluid, i.e., supercritical carbon dioxide (sCO_2) as opposed to traditional steam. sCO_2-based power cycles have the potential to exhibit superior thermal efficiencies compared to the traditional steam-based cycles. sCO_2 exhibits non-flammability and chemical stability at elevated temperatures. The process of CO_2 condensation during heat rejection facilitates seamless integration with heating and cooling systems, hence enabling the combined, generation of power and heating/cooling functionalities.

The integration of sCO_2-based power cycles into the CSP technology shows promising outcomes towards the DOE's goals of levelized cost of electricity (LCoE) of $0.05/kWh [13]. The heat transfer media (HTM) research is divided in three categories/ pathways: (1) liquid pathway (molten salts), (2) particle pathway, and (3) gas phase pathway, among which, the particle pathway is considered the most promising. Further technology maturation in the particle pathway is subjected to some challenges, which includes the difficulty in efficiently heating the particles at the solar receiver, efficiently extracting the thermal energy from the particles and its transfer to the cold side of the heat exchanger, erosion, attrition, conveyance, and parasitic loss. In addition to that, ceramic particles that are known for their high solar absorptivity and thermal stability, tend to have low intrinsic thermal conductivity [15,16]. Due to the low thermal conductivity,

significant improvements in heat transfer at the particle side of the heat exchanger are required to maximize the performance of the particle-to-sCO_2 heat exchanger and hence boost the power plant's efficiency. One of the configurations for particle-to-sCO_2 heat exchanger, is shell-and-plate, where particles move between adjacent parallel plates under the influence of gravity in a packed bed manner and is commonly known as moving packed bed heat exchanger (MPBHE) [17]. Note that MPBHEs can also be found in shell-and-tube configurations, however, the shell-and-plate configuration is considered more suitable than the former, in terms of factors such as, cost, heat transfer, structural reliability, manufacturability, parasitic losses, scalability, erosion etc. [18].

The MPBHEs are widely utilized in a variety of applications including heat recovery, solid drying, filtration, and thermochemical conversion [19]. In context with particle-to-sCO_2 heat exchangers, the heat exchanged between the moving packed bed with the parallel plates is poor, due to low inherent thermal conductivity of the packed bed of particles in motion, improper contact between particles and walls, and void space between the particles even in moving packed bed configuration. Fang et al. [20] explored a parallel shell-and-plate design, and found that the distance between the heat transfer plates (channel width) significantly influences the heat transfer between the particles and the fluid. The authors observed that narrow channel leads to a higher local heat transfer coefficient. Isaza et al. [21,22] presented analytical solutions for the heat transfer in parallel plate heat exchanger in both co-current [21] and counter-current configurations [22], under simplified conditions where the moving solid bed was considered as a homogeneous medium under local thermal equilibrium. The results underscored the impact of the Biot number on the temperature gradient near the walls, highlighting the importance of particles' effective thermal conductivity on the heat exchanger's performance. The study also affirmed that a smaller width between the plates enhances the heat transfer coefficient. However, flow visualization revealed that extremely narrow distances between the plates could lead to temporary particle bridging, impeding the flow which leads to poor heat transfer performance. Besides the plate width, the particle thermal conductivity and void fraction were found to significantly affect the thermal performance of a parallel plate heat exchanger.

Yin et al. [23] demonstrated that an increase in particle diameter resulted in increased effective thermal conductivity of the packed bed, albeit at the expense of a reduced overall heat transfer coefficient. Conversely, a higher particle void fraction led to a decrease in both the effective thermal conductivity and the overall heat transfer coefficient. An experimental study by Maskalunas et al. [24] showed that a heat transfer coefficient of 350 W/m^2K can be achieved. The experiments were conducted with silica sand particles of varying diameters moving between heated parallel plates, simplified the measurement of the heat transfer coefficient as it obviated the need for heating the particles. Despite the promising findings, most research on parallel plate heat exchangers has primarily focused on the effects of particle properties and the distance between the plates, leaving room for further exploration. The simplicity of the parallel plate heat exchanger design makes it a promising candidate for their implementation in CSP power plants' particle-to-sCO_2 heat exchangers. However, as mentioned above, the convective heat transfer between the MPB and parallel plates is generally low. Further, a long parallel plate

channel leads to the development of thermal boundary layer, which increases in size, resulting in inferior heat transfer. One way to address this issue was proposed in [17] through incorporation of smaller banks, however, this design feature comes at a significant upfront cost, as well as higher accumulated operational and maintenance costs.

Literature review suggests that low heat transfer coefficient on the particle side is considered a *bottleneck* in the employment of shell-and-plate configuration with MPB for particle-to-sCO_2 heat exchanger. The particle side thermal transport can be increased by modifying the parallel plate configuration for a fixed channel width. The first design consideration is channel width since particle heat transfer significantly depends on this factor. This parameter also affects the reliability in the particles' flowability, if reduced below a certain level for a given particle size distribution. To this end, particle channel widths between 4-10 mm have potential, as currently, the most explored particle diameter varies between 100-500 microns. Now, for a certain channel width, the parallel plate domain needs to be modified, to achieve higher thermal transport. One way to enhance heat transfer between the moving packed and the parallel plates, is to install obstacles/bluff bodies such that particles interact with them and move around them, which causes local velocity enhancement and increases the conjugate heat transfer capabilities. Although there have been some limited computational studies on understanding the MPB flow around obstructions, they are mostly inspired by the shell-and-tube arrangement, where particles move in the shell and the tubes carry a suitable working fluid. In a shell-and-plate configuration, particles moving between two parallel plates and secondary fluid to which heat is to be transferred moves in minichannels bonded on the parallel plates. The fundamental studies on MPB around obstructions can be leveraged to develop advanced concepts for shell-and-plate particle-to-sCO_2 heat exchanger, with a focus on enhancing the particle-side heat transfer coefficient.

Deng et al. [25] carried out experimental and numerical study on MPB of particles through staggered arrangement of circular tubes. Through discrete element modeling (DEM), the high and low velocity zones of particles were identified, where typically, the zones above the pins had low particle flow velocities, while particles moved faster in between two adjacent pins. An experimental study was conducted by Dai et al. [26], where the authors studied the movement of three types of particles, with one of them being glass beads, around circular obstruction. A similar trend on high and low velocity zones as observed in [25] was observed by the authors in [26]. In [26], the void zones were also identified around the circular obstruction, where particles were not present. Such zones are detrimental to heat exchange between particles and circular walls. A combined particle image velocimetry (PIV) and DEM study was carried out by Bartsch and Zunft [27], where this void region just downstream of the cylindrical pin was studied in detail for a staggered arrangement of cylindrical obstructions. It was shown that particle velocity increased around the sides of the cylinders, while two distinct low heat transfer zones were also identified. These zones correspond to the area right above the cylinders where particle motion is effectively non-existent, and the other zones is the region right downstream of the cylinders which does not even feature particles. These zones can be called 'dead/stagnant' and 'void' zones, respectively. One approach to address the so

called ‘dead’ and ‘void’ zones is to modify the circular profile of the obstruction. Tian et al. [28] studied circular, elliptical and hexagonal tubes through DEM, to characterize the MPB flow and heat transfer around these obstructions. The elliptical shape alleviated some of the stagnation concerns, while significantly improving the void zone, particularly when the ellipse was elongated in the direction of MPB. In a follow-up study, the authors in [28] carried out a DEM study [29] on a trapezoidal obstruction with smoothened corners, and reported a 14% increase in heat transfer compared to parallel plate.

Literature review on the methods to enhance heat transfer between moving packed bed through obstruction suggests that very limited studies have been carried out, with most studies on shell-and-tube configuration which involves long tubes resulting in two-dimensional flow around the tubes. The studies carried out on the obstructions in context with the shell-and-plate heat exchangers, where a solid pin joins the two parallel plates, are also sparse, and largely limited to computations. Furthermore, the effect of spacing of two parallel plates on heat transfer is profound, and this aspect is not studied in reference to obstructions’ employment in closely spaced parallel plates.

6. Project Objectives:

The project is aimed towards the design and development of porous channels for falling particles in order to increase the heat transfer coefficient on the particle side and hence increase the overall heat transfer coefficient of particle-to-sCO2 heat exchangers. The above objective will be demonstrated through increase in both the effective thermal conductivity of the falling particle channel and the interstitial heat transfer coefficient between the particles and the fibers. The overarching goal of this project is to provide pathway to reduce the levelized cost of electricity by utilizing concentrated solar thermal power.

Task 1.0: Heat transfer characterization of high-porosity metallic foams

Flow experiments at different Reynolds number to measure Interstitial heat transfer coefficient (hsf), defined as unit cell length scale heat transfer coefficient based on local wall heat flux (q"w), local wall temperature (Tw,x) and local fluid temperature (Tf,x). This quantity is inclusive of the conjugate heat transfer aspects at both fiber and lattice endwall. Pressure drop measurements to determine permeability (K) and inertial coefficient (Cf) through a regression analysis. ASTM E1225-20 experiments for effective thermal conductivity (keff) of the particle bed measurements will also be performed.

The output of this task will be a complete thermal characterization of metallic foams which will be additively manufactured in different metallic alloys. The uncertainty in hsf and keff <5%. via sequential perturbation method. The keff characterization will be carried out for porosities ranging from (0.75, 0.9). The hsf measurements will be carried out for flow Reynolds numbers ranging from 2,500-10,000 and Pr - 0.717. ASTM E1225-20. The success criterion will be assessed through the comparison of hsf correlation for conventional foams with literature. Validation of in-house LBM computation with in-house experiments and correlations from literature. Benchmarking experimental and numerical model for air- and particle-based flow media.

Task 2.0: Numerical optimization and experimental demonstration of advanced heat exchanger performance.

In this task, validated numerical model from Task 1 will be used to carry out large scale computations to optimize the counterflow heat exchanger configurations featuring Octet-shape based cellular structures on the hot side, and air in the cold side. For a fixed heat exchanger prototype configuration, the dimensions of the mini-channels of the cold side and the representative particle side dimension-space will be decided, based on the computational optimization. The optimization design variables include porosity, particle channel size and particle size. Experiments will be carried out to support the computational results and U versus Δp relationship will be established for a wide range of hot and cold side flow conditions, with particle flow included on the hot side. Particle temperatures are expected to reach about 200 °C.

Task 3.0: Test bench experiments.

Provide particle-to-sCO2 HX testing to measure the performance of the prototype heat exchanger designed and fabricated by MSU. This test program will aim to demonstrate the Up enhancement>100% and its subsequent effect on UHX enhancement (to be determined with sCO2 tests) consistent with MSU lab-scale results.

Task 4.0: Cost analysis of enhanced heat exchanger performance.

In collaboration with stakeholders, we will develop cost correlations for specific nuances of the additive, Octet fiber technology compared to a parallel plate baseline. Generalized cost modeling for heat exchanger performance metrics. Cost of the Heat Exchanger per kW size ($/kW) Constraint: Particle T inlet <500 C; sCO2 inlet =to be determined based on revised HX performance; sCO2 outlet > 450 C; Particle T outlet =to be determined based on revised HX performance to be determined based on revised HX performance.

Milestone #	Anticipated Month of completion	Performance Metric	Assessment Tool / Method of Measuring Success Value	Verification Process
1.1	1st (0-1 month)	h_{sf}, k_{eff}, K, C_f	In-house temperature and pressure gradient measurements / comparing h_{sf}, k_{eff} of TKD experiments with existing correlation.	With prescribed range of Re and ks, a validation within $\pm 10\%$ with correlation will verify the success values and benchmark the experimental facilities.
1.2	2nd (0-2 months)	h_{sf}, k_{eff}, K, C_f	Demonstrate independence of hsf and keff on thermal boundary conditions.	Multiple heat flux measurements. X-Ray tomography on randomly chosen

Milestone #	Anticipated Month of completion	Performance Metric	Assessment Tool / Method of Measuring Success Value	Verification Process
			Experiment repeatability within 2%. with measurement uncertainty < +/-5%. Deviation in AM samples above measurements< +/-2% to pass the criteria for heat transfer testing.	samples for pore and fiber shape/size assessment.
1.3	3	h_{sf}, k_{eff}, K, C_f	k_{eff} (LBM) validation for ε -> (0.75,0.9). h_{sf} (LBM) validation for Re-> (2,500-10,000) with experimental database generated in Task 1.1-1.2	Continuous feedback from in-house measurements, uncertainties.
1.4	3rd (2-3 months)	Bi-weekly meetings and email communications.	1) Meeting Minutes Exist 2) FMEA formalism.	Involvement of project partners at design stage and in measurement plans, LBM strategy, with over-arching goal to guide sub-section developments towards employment of HX concept in 20 kW HX test facility at SNL.
2.1	9th (4-9 months)	U_p, U_{HX}, η, Δp	(1) A thorough check of heat exchanger analysis through control volume approach, IR measurements, thermocouple measurements in the skin of the plates encompassing porous media. (2) Estimate uncertainties associated with U_p and U_{HX} with a 95% confidence interval based on a t-distribution.	Comparison with Task 2.2 experimental measurements on selected configurations from optimization program.

Milestone #	Anticipated Month of completion	Performance Metric	Assessment Tool / Method of Measuring Success Value	Verification Process
			(3) Validate that the calculated values of U_p and U_{HX} from Task 2.2 fall within the confidence interval with 95% confidence level.	
2.2	9th (4-9 months)	U_p, U_{HX}, η, Δp	(1) Baseline U_{HX} (plane channel without metal foam) matching with correlations within +/- 10%. (2) U_p and U_{HX} calculated in this task fall within the confidence interval estimated in Task 2.1 with 95% confidence level.	Comparison of U_{HX} and Δp measurements on baseline configuration with correlations.
2.3	12th (4-12 months)	Performance mapping of local heat transfer and global heat transfer exists over specified Operational Variables.	Methodology described in Ma and Martinek. Heat exchanger performance tabulation and correlation development for modular HX.	Comparison with prior cost analysis reports, with technical paper and with conventional heat exchangers. Report writing, technical manuscript preparation for dissemination to DOE and other scientific communities.
3	12th	U_p, U_{HX}, η, Δp	The experimental data to be evaluated against SNL's publications to quantify the gains in Up, UHX with respect to pumping power.	Through comparative analysis with existing database in prior projects/ computational results from 2.1. [1] Albrecht, K.J. and Ho, C.K., 2019. Design and operating

Milestone #	Anticipated Month of completion	Performance Metric	Assessment Tool / Method of Measuring Success Value	Verification Process
				considerations for a shell-and-plate, moving packed-bed, particle-to-sCO2 heat exchanger. *Solar Energy*, *178*, pp.331-340. [2] Albrecht, K.J., et al., "Testing and Model Validation of a Prototype Moving Packed-Bed Particle-to-sCO2 Heat Exchanger", SolarPACES 2019, Daegu, South Korea 2019.
4	12th	$/UA	Methodology described in Ma and Martinek.	Cost of the Heat Exchanger per kW size ($/kW) Constraint: Particle T_{inlet} <500°C; sCO_2 inlet =to be determined based on revised HX performance; sCO_2 outlet > 450°C; Particle T_{outlet} =to be determined based on revised HX performance to be determined based on revised HX performance

7. Project Results and Discussion:

We have carried out detailed heat transfer and fluid flow experiments on additively manufactured lattice frame materials in SS420 based on Octet unit cells. Our experiments

have yielded in interstitial heat transfer coefficient as a function of flow velocity, effective thermal conductivity, permeability, and inertial coefficient. With these four parameters, one can find the heat exchanger performance and the cost.

Before reporting above parameters, firstly we present characterization of the AM parts. For the effective thermal conductivity part, we have printed Octet samples in SS420 and SS316L.

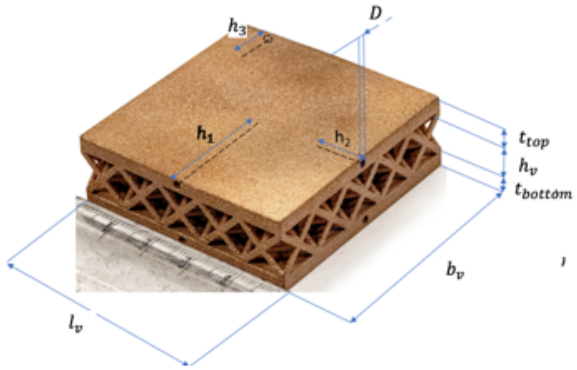

$$\varepsilon = \frac{\forall_{air}}{l_v b_v h_v} = 1 - \frac{\forall_{metal,lattice}}{l_v b_v h_v}$$

$$\forall_{metal,lattice} = \frac{m_{metal,lattice}}{\rho_s} = \frac{m_{total} - m_{walls}}{\rho_s}$$

$$m_{walls} = \rho_s[l_v b_v(t_{top} + t_{bottom}) - 2(\pi D^2/4)(h_1 + h_2 + h_3)]$$

Fig. 1 AM structure, important dimensions' nomenclature, porosity calculations

Tables 1 and 2 show the dimensions identified in Fig. 1 along with the percentage deviations. These deviations have a cumulative effect on the parts performance in terms of heat transfer and pressure drop and the actual porosity.

Table 1 Deviations in SS420 parts

		SS420_0.75			SS420_0.8			SS420_0.88		
		Intended (mm)	Measured (mm)	Deviation %	Intended (mm)	Measured (mm)	Deviation %	Intended (mm)	Measured (mm)	Deviation %
	h_v	10.00	9.91	**0.94**	10.00	9.73	**2.72**	10.00	9.86	**1.45**
Top wall	l_v	50.80	50.19	**1.20**	50.80	50.29	**1.00**	50.80	50.24	**1.10**
	b_v	50.80	49.96	**1.65**	50.80	49.99	**1.60**	50.80	50.39	**0.80**
	t_{top}	3.18	3.40	**7.20**	3.18	3.43	**8.00**	3.18	3.28	**3.20**
	h_1	25.40	24.82	**2.30**	25.40	24.87	**2.10**	25.40	24.97	**1.70**
	h_2	8.46	8.59	**1.50**	8.46	9.12	**7.81**	8.46	8.53	**0.90**
	h_3	8.46	8.53	**0.90**	8.46	9.53	**12.61**	8.46	8.43	**0.30**
Bottom wall	l_v	50.80	49.94	**1.70**	50.80	49.89	**1.80**	50.80	50.50	**0.60**
	b_v	50.80	49.99	**1.60**	50.80	49.91	**1.75**	50.80	50.42	**0.75**
	t_{bottom}	3.18	3.25	**2.40**	3.18	3.30	**4.00**	3.18	3.51	**10.40**
	h_1	25.40	24.77	**2.50**	25.40	24.87	**2.10**	25.40	25.27	**0.50**
	h_2	8.46	8.71	**3.00**	8.46	8.79	**3.90**	8.46	8.51	**0.60**
	h_3	8.46	8.53	**0.90**	8.46	8.66	**2.40**	8.46	8.31	**1.80**

Table 2 Deviations in SS316L parts

		SS316_0.75			SS316_0.8			SS316_0.88		
		Intended (mm)	Measured (mm)	Deviation %	Intended (mm)	Measured (mm)	Deviation %	Intended (mm)	Measured (mm)	Deviation %
	h_v	10.00	9.75	**2.46**	10.00	9.70	**2.97**	10.00	9.73	**2.72**
Top wall	l_v	50.80	47.85	**5.80**	50.80	47.75	**6.00**	50.80	48.41	**4.70**
	b_v	50.80	47.78	**5.95**	50.80	47.68	**6.15**	50.80	48.36	**4.80**
	t_{top}	3.18	3.12	**1.60**	3.18	3.10	**2.40**	3.18	3.15	**0.80**
	h_1	25.40	24.36	**4.10**	25.40	14.91	**41.30**	25.40	18.06	**28.90**
	h_2	8.46	8.05	**4.80**	8.46	7.92	**6.31**	8.46	8.41	**0.60**
	h_3	8.46	6.78	**19.82**	8.46	7.72	**8.71**	8.46	3.18	**62.46**
Bottom wall	l_v	50.80	48.23	**5.05**	50.80	47.80	**5.90**	50.80	47.63	**6.25**
	b_v	50.80	48.13	**5.25**	50.80	47.73	**6.05**	50.80	47.73	**6.05**
	t_{bottom}	3.18	3.10	**2.40**	3.18	3.18	**0.00**	3.18	3.10	**2.40**
	h_1	25.40	21.77	**14.30**	25.40	11.76	**53.70**	25.40	24.00	**5.50**
	h_2	8.46	7.98	**5.71**	8.46	7.92	**6.31**	8.46	8.51	**0.60**
	h_3	8.46	7.85	**7.21**	8.46	7.95	**6.01**	8.46	3.94	**53.45**

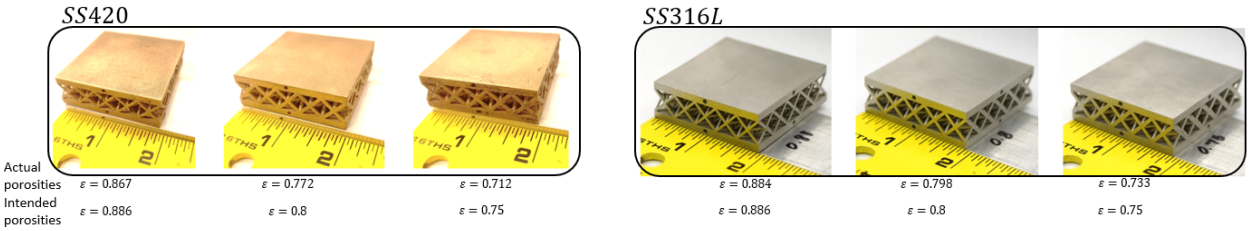

Fig. 2 Actual versus Intended porosities of the AM structures in SS420 and SS316L

Figure 1 shows a sample of the AM part in SS420 along with the nomenclature of important dimensions and porosity calculation methodology. The reason for such detailed characterization is the deviations we expect based on our past experience, in terms of resultant porosity versus the intended one. Figure 2 shows the three different porosities of each SS420 and SS316L along with the actual porosity values. In our plan, we are covering lattices with porosities ranging from 0.75 to 0.886. It can be seen that the porosity of the AM parts are slightly different from the intended ones, and we have taken a note of this behavior in our future design based decisions.

Figure 3 shows the detailed CT scan data of an AM part (SS420) at intended porosity of 0.886. It can be seen that for the unit cell thickness of 10 mm, the roughness length scales at the fiber and endwalls are significant and are expected to have an effect on the flow and thermal transport through the lattices, as well as particle packing efficiency which is discussed later. Further, we can observe defects at certain locations where fibers merging at a junction.

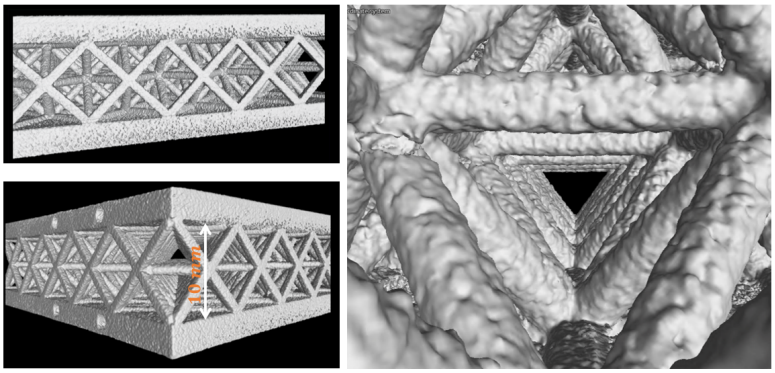

Fig. 3 CT scan data of the Octet sample (intended porosity – 0.886)

Effective Thermal Conductivity (k_{eff}) of lattices

One of our hypotheses in achieving enhanced overall heat transfer coefficient of heat exchanger where the hot side channel is equipped with lattices, is the enhancement in k_{eff}. To this end, this section presents the details of the experimental setup built for k_{eff} measurements.

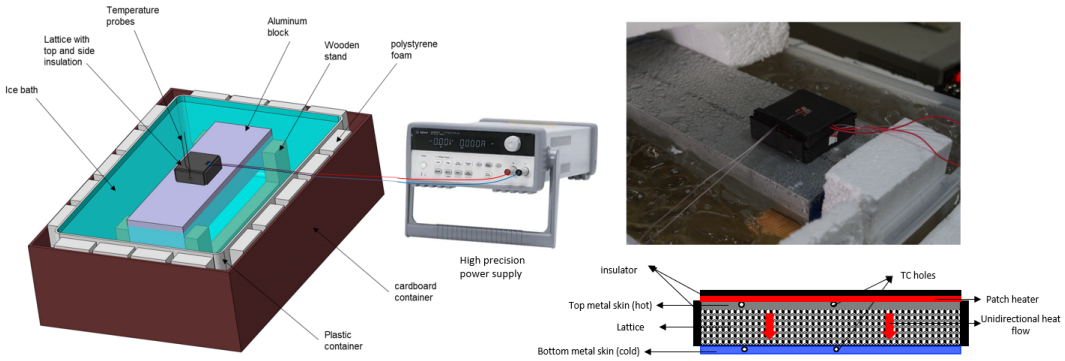

Fig. 4 Experimental setup for k_{eff} measurements

$$k_{eff} = \frac{(q/A)\Delta z}{\Delta T} = \frac{(q_{total} - \sum q_{loss}/A)\Delta z}{\tilde{T}_{top} - \tilde{T}_{bot}}$$

$$\sum q_{loss} = \frac{k_{ins}}{t_{ins}}\left[A\left(T_{Top,in} - T_{Top,out}\right) + 4b\Delta z\left(T_{side,in} - T_{side,out}\right)\right]$$

Steady-state experiments were conducted to evaluate the k_{eff} of the lattice samples with air as the fluid phase. Single-cell thick lattices were printed to calculate the k_{eff} of each topology with unit cell size of ~ 10 mm. The overall dimension of the lattice was ~ 50 mm x 50 mm x 10 mm (l x w x h) that was sandwiched between 3.175 mm thick substrate walls. Patch heaters were pasted on one of the substrate plates and the backside of the heater was insulated using low thermal conductivity Styrofoam. The four side-faces of the samples were also insulated to prevent the losses. The sample and heater assembly was placed on a copper block having dimensions of about 100 mm x 100 mm x 25.4 mm which demonstrated high thermal mass. The Aluminum slab was partially submerged in a reservoir containing recirculating ice-water slurry with the help of supporting legs. The recirculation of the water in the reservoir ensured that the heat transferred from the copper block was mixed well. The substrate plate temperatures were recorded at the circular slots provided for thermocouple measurements. Since the samples were printed in SS420 infiltrated with Bronze through Binder Jetting process, it is important to accurately measure the solid material thermal conductivity (k_s). The in-house measurements of the solid sample of SS420 yielded k_s equal to 20.8 W/mK and for SS316L, the was k_s 13 W/mK.

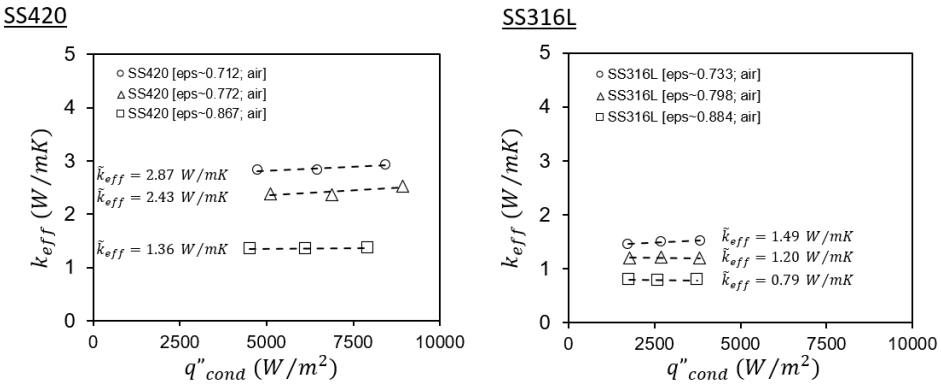

Fig. 5 Effective thermal conductivity of SS420 and SS316L lattices for different porosities and heat flux levels.

The effective thermal conductivity experiments were carried out at three different heat flux levels to demonstrate that the reported values are in turn independent of the thermal boundary condition. It was ensured that the lattice temperature was close to the room temperature since thermo-physical properties start to significantly change at elevated temperatures. There have been studies focused on the effect of temperature on the effective thermal conductivity, however, this aspect was out of scope in our study. Through literature search, we observe that k_{eff} increases wit the temperature levels.

Figure 5 shows the k_{eff} values of SS420 and SS316L. It can be observed that the k_{eff} values were nearly constant with respect to the applied heat flux. SS420 lattice was nearly twice as conductive as SS316 for the lowest porosity case. Note that the relative porosities of the two samples were different due to the AM process and has been listed in the legends. Porosity has a significant effect on the resultant k_{eff}.

In our Lattice Boltzmann simulation effort to characterize the effective thermal conductivity for lattice frame materials, we carried out a comprehensive parametric analysis by varying all parameters which effect k_{eff}, for example, solid and fluid phase thermal conductivities, porosity. We also proposed a generalized correlation for k_{eff} of the Octet structure given by the following equation.

$$\frac{k_{eff}}{k_s} = 0.7397\varepsilon^2 + \left(\frac{k_f}{k_s} - 1.7397\right)\varepsilon + 1$$

Figure 6 below shows the comparison of the experimental data (Fig. 5) for SS316L and SS420 with the correlation from the validated LBM model. Also, we used our correlation presented make projections for comparison with lattice performance with AlSi10Mg which is alloy closer to the Aluminum foam properties (which was investigated in Task 1.1). It can be seen that for critical porosities below 0.84, our targets are met. Hence, considering both flow and heat transfer milestone metrics, we are looking at a designed porosity of 0.84 for further research and development. The porosity values of future parts in Task 1.2 and 2.1 will also be subjected to the manufacturing constraints.

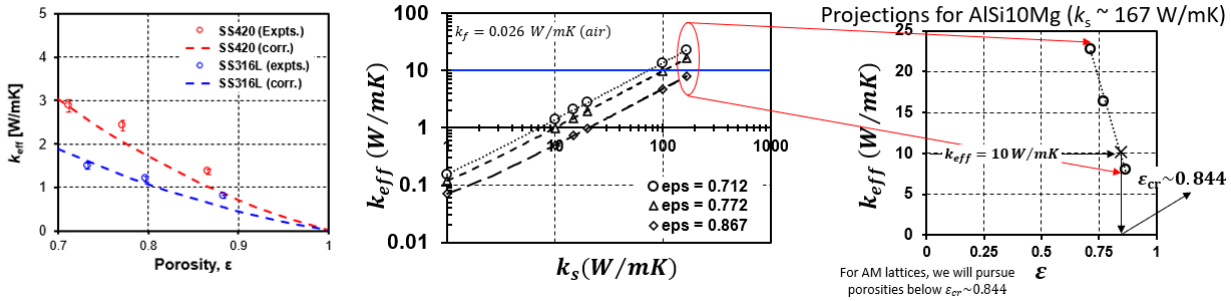

Fig. 6 Comparison of experimental data on k_{eff} for two different k_s values with correlation prescribed in our paper [3], also shown is the analysis for k_{eff} vs k_s variation and projections for AlSi10Mg (k_s~167 W/mK).

Characterization of particles

This section describes our characterization efforts on different particles we have tested so far. In the proposed concept, falling particles in presence of lattice will exchange higher heat with the solid media due to benefits in both resultant increase in effective thermal conductivity and particle-to-fiber interaction. Note that in Figs. 5 and 6, the k_{eff} was reported for lattices with void space occupied by air ($k_s = 0.026\ W/mK$). Prior to reporting k_{eff} of lattices packed with particles, it is important to look into the particle size distribution and the particle packing efficiency in the presence of lattice and in default packed bed scenarios.

We initially started working on bauxite particles from AGSCO. Some important properties from manufacturer are provided below. Tables 3 shows the physical properties and chemical composition of AGSCO bauxite particles. Further, we also outsourced the measurements of particle size distribution through laser diffraction method using Anton Paar PSA1190. Particles were launched into the laser beam with the help of compressed air. The laser beam diffracts when a small particle passes through it, creating a pattern at the receiver located at the other end of the PSA. The receiver sends the diffraction pattern to the processing unit where it gets converted into particle size sing Mie or Fraunhofer models.

Table 3 AGSCO bauxite particle physical properties and chemical composition

TYPICAL PHYSICAL PROPERTIES

Specific Gravity	3.15 g/cm^3
Average Packing Density	1.85 g/c m^3
Pore Volume	0.035 g/cm^3
Median pore diameter	69 microns
Shape	Sphericity (0.9 Krumbein) Roundness (0.9 Krumbein)
Hardness	Knoop - 754 Kg/mm^2 (1 Kg load)
Specific Heat	0.20 cal/g/^{O}C
Heat Stability	>1200 ^{O}C (First liquid phase)
Acid Solubility (API)	2.5% loss in 12%HCl / 3%HF at 150 ^{O}F for 30 minutes

TYPICAL CHEMICAL ANALYSIS

ALUMINUM OXIDE	(Al_2O_3)	73.9 %
SILICON DIOXIDE	(SiO_2)	16.5 %
IRON OXIDE	(Fe_2O_3)	5.5 %
TITANIUM DIOXIDE	(TiO_2)	3.6 %
MANGANESE OXIDE	(MnO_2)	0.15%
CALCIUM OXIDE	(CaO)	0.15%
SODIUM OXIDE	(Na_2O)	0.10%
POTASIUM OXIDE	(K_2O)	0.10%

Particle Size Distribution

Figure 7 shows main components of the particle size analyzer and its working principle. In our study, the particle size distribution has a significant role, apart from its thermo-physical properties, since that essentially determines the particle packing fraction or simply put the revised porosity of the lattice when packed with particles.

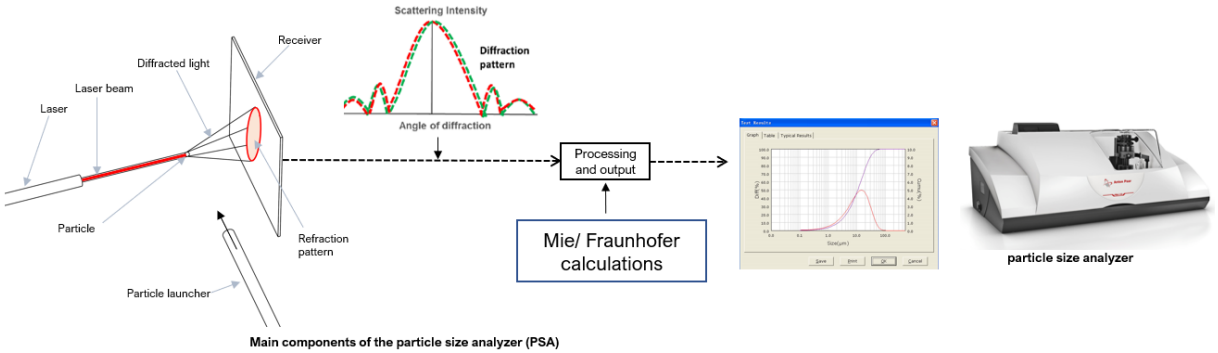

Fig. 7 Main components of particle size analyzer (PSA)

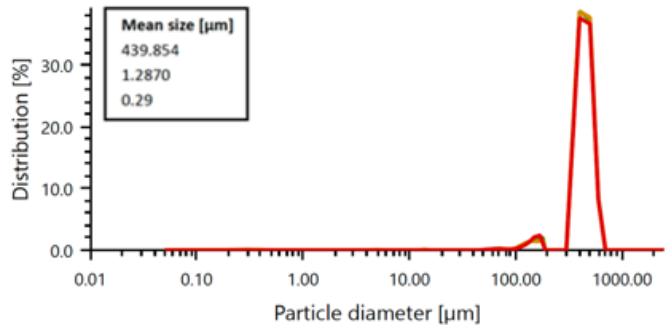

Fig. 8 Particle size distribution for AGSCO bauxite

Figure 8 shows the particle size distribution of the AGSCO bauxite particles which were tested initially. The mean size of AGSCO particles was 439 microns.

The particle size distribution of CARBOBEAD-HSP 20/40, CARBOBEAD-CP 30/60, CARBOBEAD-CP 40/100 particles are shown below.

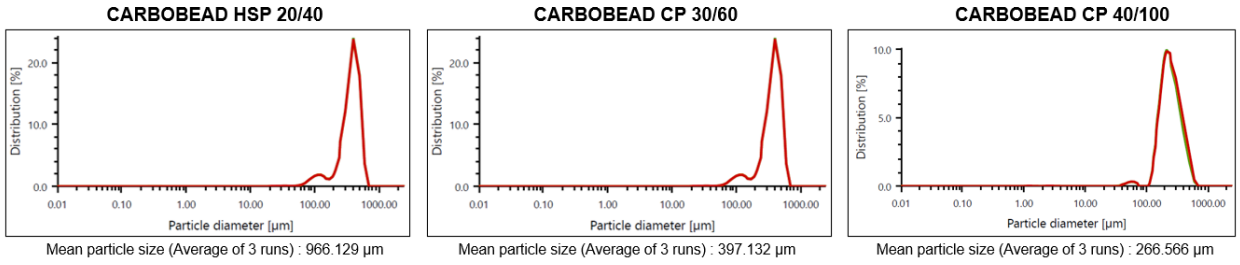

Fig. 9 Particle size distribution of three different types of CARBO particles

The mean particle size were 966 microns for CARBOBEAD HSP 20/40, 397 microns for CARBOBEAD-CP 30/60, 266 microns for CARBOBEAD-CP 40/100. With these batches of CARBO particles, we are essentially covering 266 – 966-micron particle sizes.

Effective Thermal Conductivity Measurements for Lattice+Particles

The k_{eff} calculation procedure is mentioned above. This section presents the k_{eff} results of lattice+particle configuration. Firstly, packed bed of particles was tested to establish the baseline for k_{eff} enhancement. Note that this is how current particle-to-sCO2 heat exchangers are based upon – particle flow through empty plain channels. Figure 14 shows the k_{eff} for the AGSCO particles and the average value was found to be 0.35 W/mK. Further, k_{eff} of the three different types of CARBO particles were tested and they had similar k_{eff} ~0.4 W/mK, however definitely higher than the AGSCO particles. It is interesting to note that the particle size (CARBO) did not have any impact on the k_{eff}.

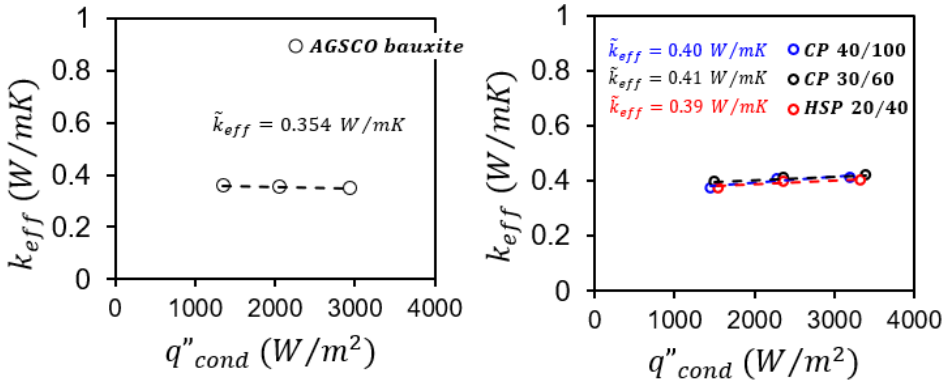

Fig. 10 k_{eff} of packed bed of AGSCO bauxite (left), three batches of CARBO particles (right)

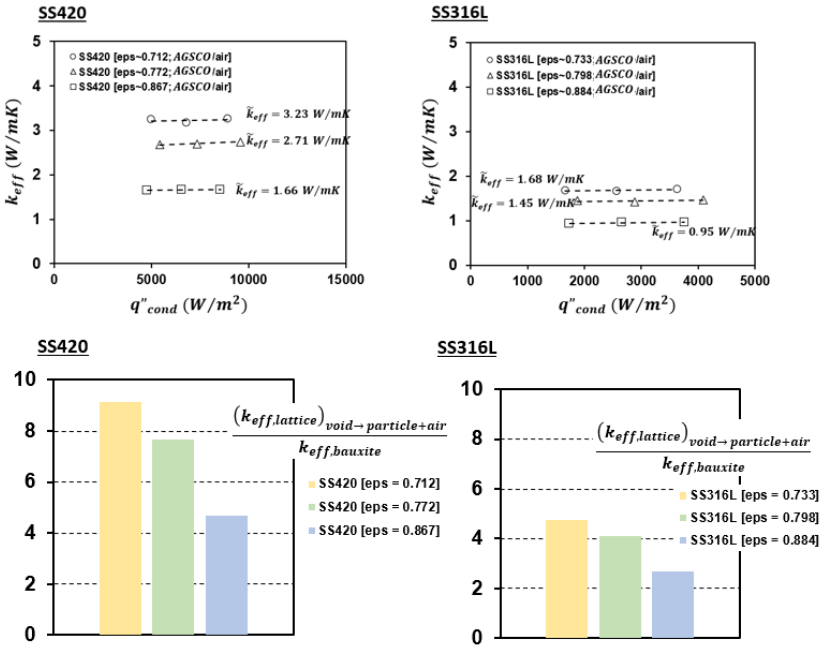

Fig. 11 AGSCO particle k_{eff} in presence of lattice and subsequent enhancement in k_{eff} in reference to packed particle bed.

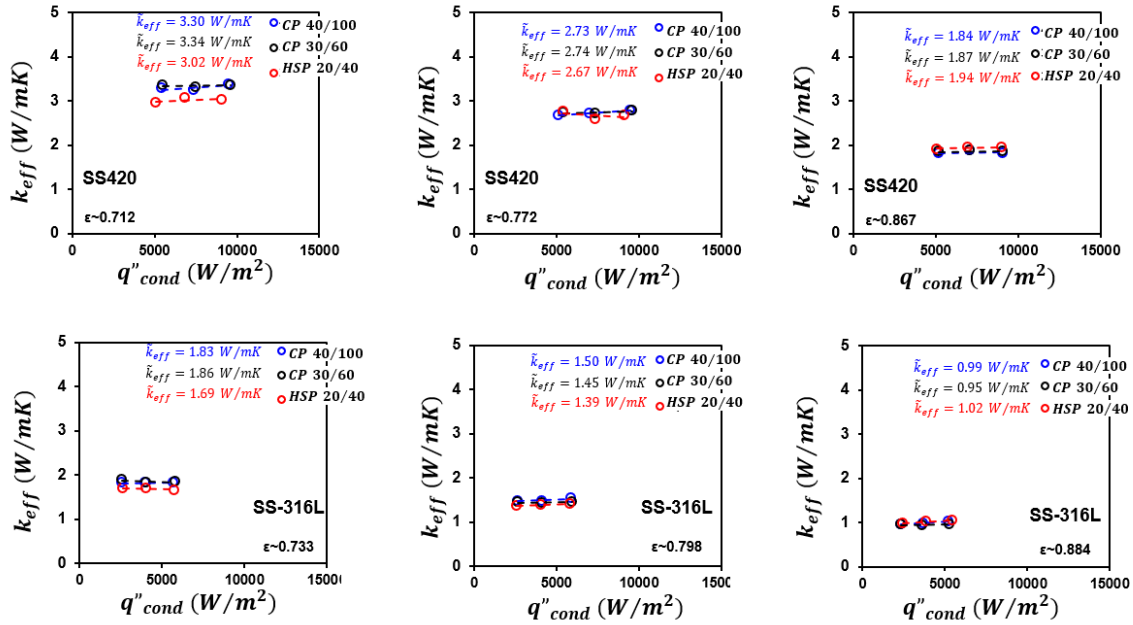

Fig. 12 CARBO particle k_{eff} in presence of lattice

Pore-scale lattice Boltzmann method (LBM) simulations

For representative test conditions and sample configurations, carry out LBM simulations. The LBM is a kinetic theory based mesoscopic numerical method that is able to preserve the complex geometry and efficient in simulating pore-scale hydrodynamics and heat transfer in porous media. The model will be validated against in-house measurements on k_{eff}, h_{sf}, K and C_f. Validated transport properties to be used in large-scale computations for heat exchanger parameter optimization.

Flow properties prediction and validation

For the present work we used the LBM model to simulate the fluid flow within the 3D periodic porous lattice structures. Periodic boundary conditions are used on the boundaries in the x, y and z directions, and no-slip boundary condition is used on the surface of solid fibers. To simulate the flow field, we applied a constant pressure gradient as a body force along the z direction. Through a regression analysis of the pressure drop versus average flow velocity profiles, the flow properties including permeability, inertial coefficient, and friction factor can be determined. Different unit-cell structures have been examined and here we focus on the Octet and Tetrakaidecahedron (TKD) structures. Octet structure is the one of most interest for the project and TKD structure is representative of traditional high-porosity metal foams.

Model Verification

Figure 14 shows the comparison between simulated normalized permeability and inertial coefficient with those in different porosities. Very good agreement with the published results is observed. From the grid independence study it can be seen that a grid resolution with unit cell length L = 150δx (δx is the unit length in the LBM scale) is sufficient.

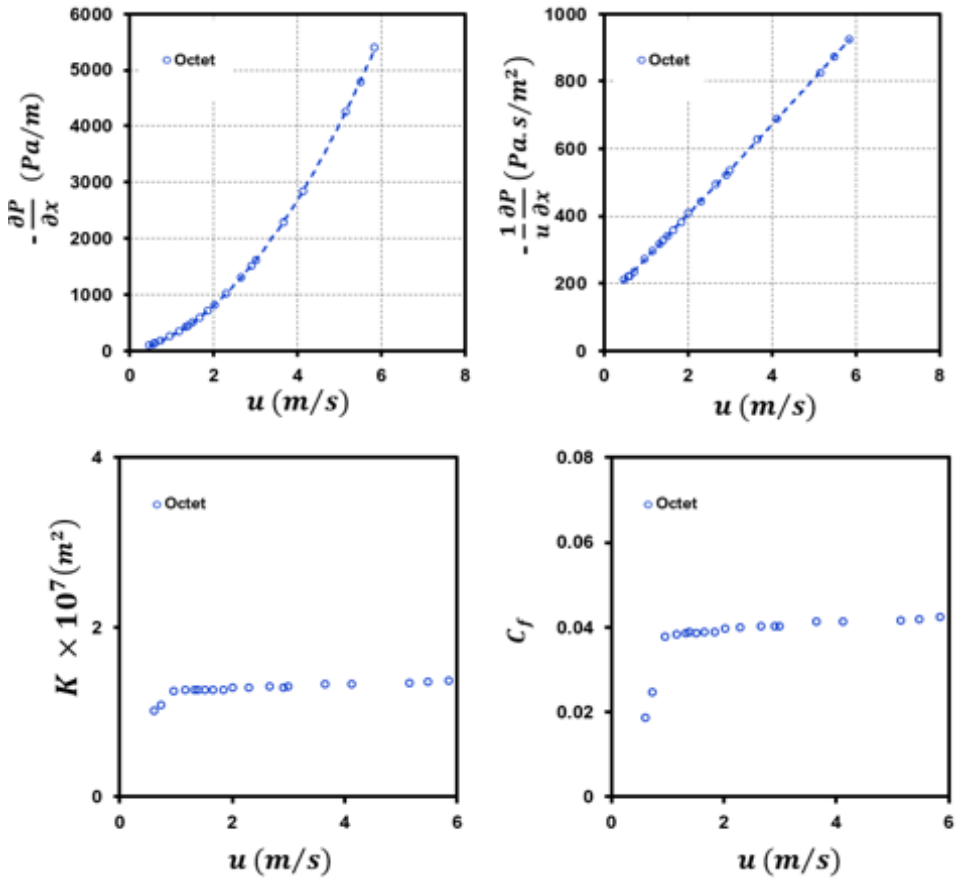

Fig. 13 Pressure drop for air flow through Octet lattice and subsequent determination of permeability and inertial coefficient (also shown is the effect of the choice of maximum temperature on K and Cf determination)

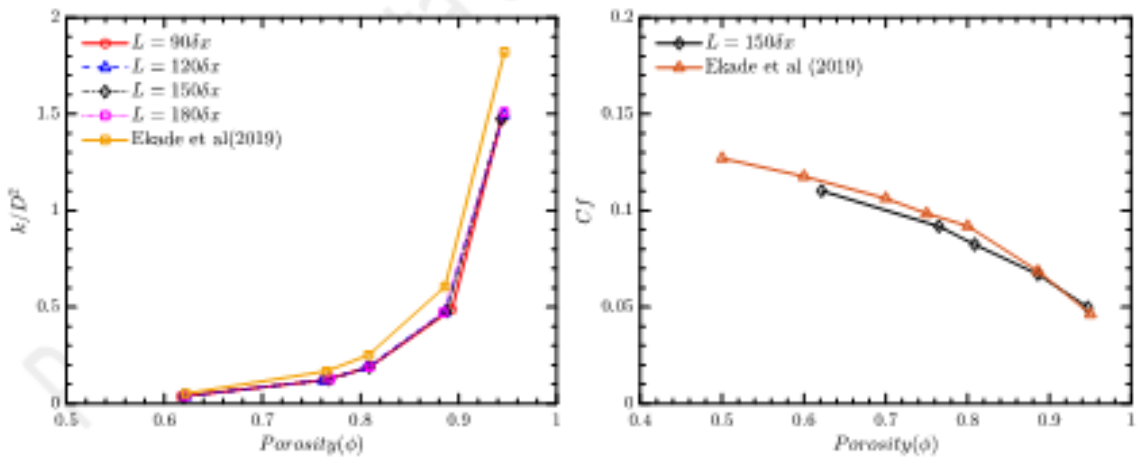

Fig. 14 (a) Normalized permeability and (b) inertial coefficient versus porosity of the additively manufactured Octet unit-cell structure.

The correlations can be used to predict the effective thermal conductivity of those structures when packed with solid particles. However, the correlation is proposed for the entire porosity range of $0 \leq \varepsilon \leq 1$, while the in-house measured porosity range of the metal foam structure is $0.7 \leq \varepsilon \leq 0.9$. Therefore, to improve the accuracy of ETC prediction, here we provide a modified correlation based on the high porosity range and the two metal pairs, i.e., SS420-air and SS316L-air,

$$\frac{k_{eff}}{k_s} = 0.6927\varepsilon^2 + \left(\frac{k_f}{k_s} - 1.6927\right)\varepsilon + 1$$

So far, the comparisons presented on k_{eff} were for the lattice alone, i.e., the void space was occupied by air. We measured k_{eff} for variety of lattice+particle combinations. Figure 16 presents a high-level comparison of k_{eff} obtained on an averaged for all three batches of CARBO particles, with in-house LBM computations leveraging our experimental data on k_{eff} of packed beds.

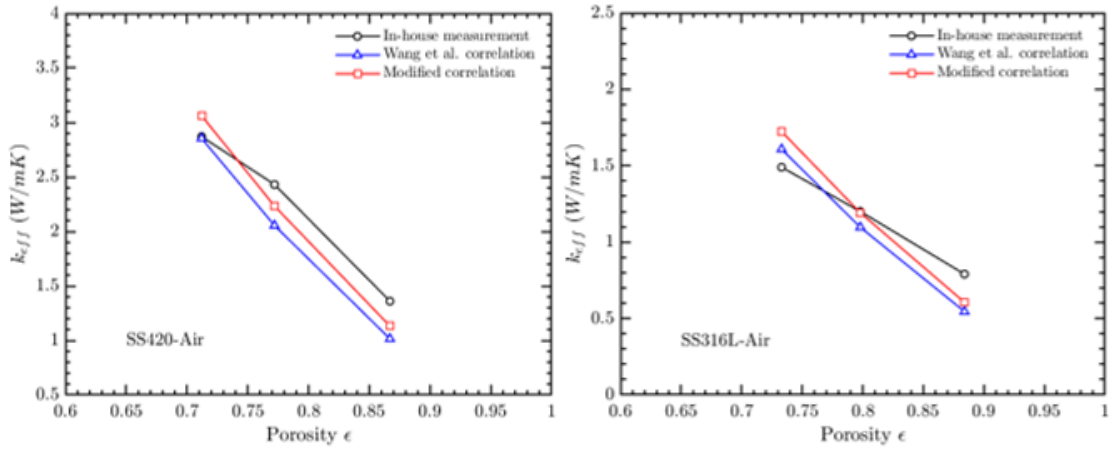

Fig. 15 (a) Comparison of the effective thermal conductivity between in-house measurement and correlations for the AM Octet structure with (a) SS420-air, and (b) SS316L-air material pairs

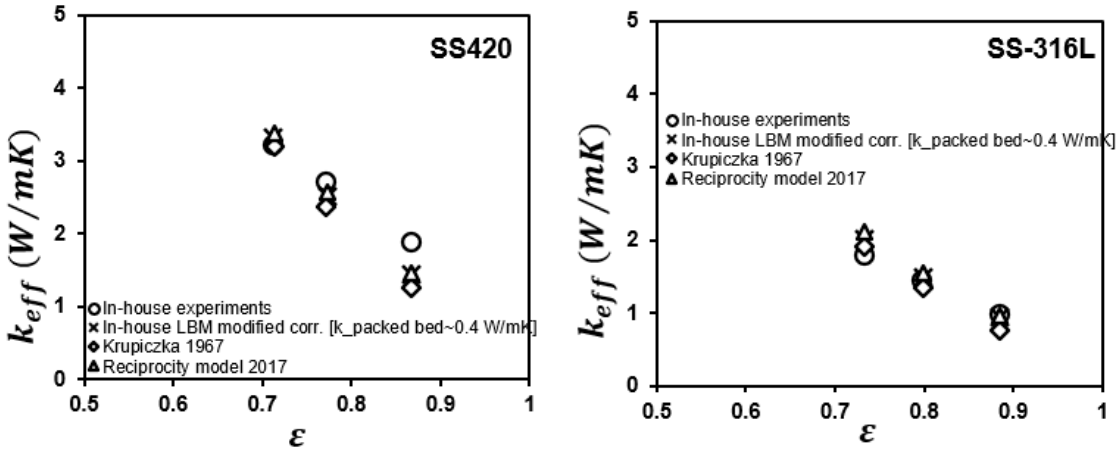

Fig. 16 Comparison of in-house experiments and LBM predictions for k_{eff} of [lattice+particles]

It is concluded from Fig. 16 that our in-house experiments and computations on k_{eff} are in good agreement with each other and LBM computations will be further extended to the next stages in this project to understand experimentally obtained thermal and flow transport data when particles will be moving through the Octet lattice.

Experimental characterization of large-scale sample made from Octet lattice structure

We have experimentally determined the convective heat transfer coefficients for air and particles as working fluids through large panels (0.15 m x 0.25 m) made from lattice frame materials in SS420 and SS316L.

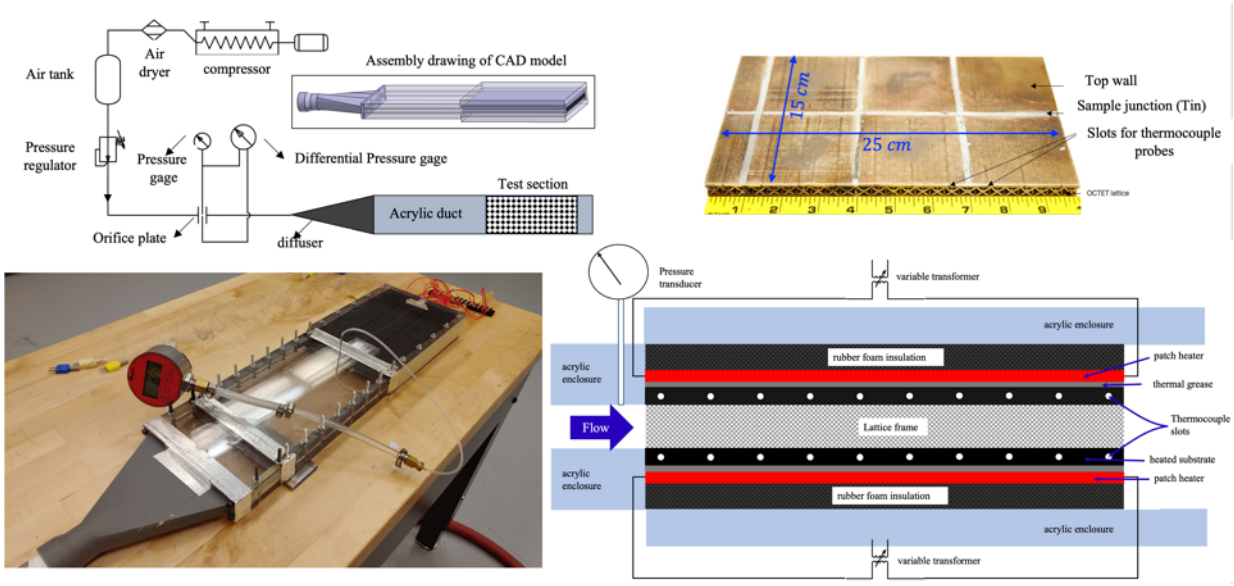

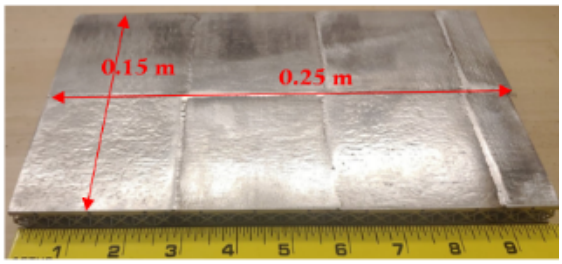

Fig. 17 Experimental setup for air-based experiments and SS420 and SS316L panels used for these experiments

The steady-state heat transfer (Fig. 17) experimental procedure included heating both top and bottom panels via the glued patch heaters and wait for the first steady state. Note that at this stage, the air flow was not switch on. Convective heat transfer coefficient at these discrete location along the streamwise direction is given as,

$$h(x) = \frac{q"_{conv}}{T_w(x) - T_f(x)}$$

where, $q"_{conv} = (q_{total} - q_{loss,insulation})/A$, and local fluid temperature, $T_f(x) = T_{f,in} + \left(q"_{conv} W/\dot{m}c_p\right)x$. The local convective heat transfer coefficient ($h(x)$) obtained from above procedure was then used to calculate a representative "h" for each row of unit cells in the streamwise direction. The air-based experiments were conducted for averaged flow velocities ranging from 3.4 to 8.4 m/s for all three lattice topologies for SS420 panels (Fig. 18). For a given lattice porosity, a developing heat transfer trend was observed closer to the inlet where the heat transfer in the first row of Octet unit cells was significantly higher compared to the ones immediately downstream. The heat transfer achieved near periodicity (i.e. it repeats itself) after 5th row and stays nearly constant for another 10 rows (with slightly increasing trend). Towards the exit, the heat transfer showed slight reduction. The two lower lattice porosities 0.75 and 0.8 had nearly similar heat transfer levels for all three velocity conditions, whereas the highest porosity 0.88 panel had distinctly lower heat transfer levels compared to the other two higher ones. This is again attributed to multiple factors which include lower effective thermal conductivity and smaller fiber diameters offering less venues of stagnation-type heat transfer enhancement as compared to the larger diameter configurations. The aim of these experiments was to quantify both the developing and developed behavior of the Octet cell rows in terms of the heat transfer enhancement.

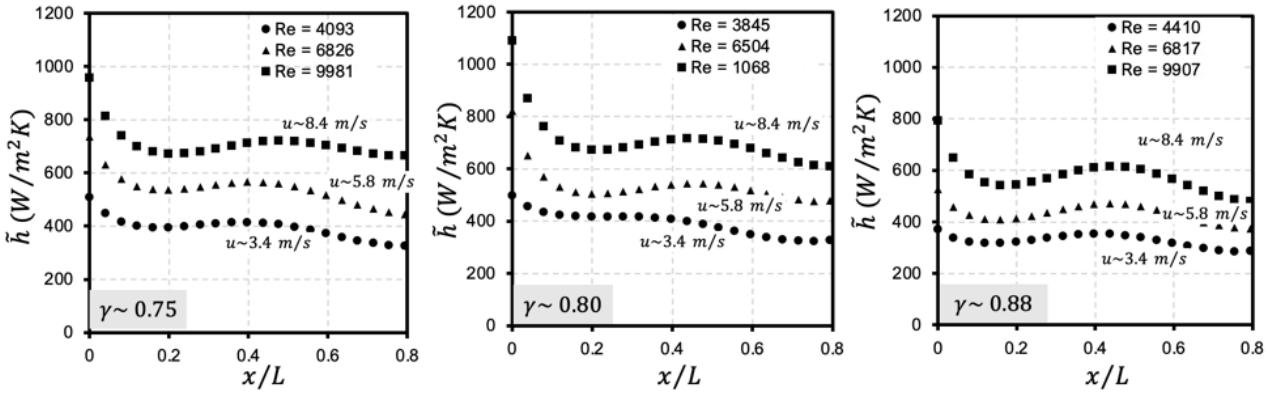

Fig. 18 Local convective heat transfer coefficient variation with lattice porosity [SS420 panels]

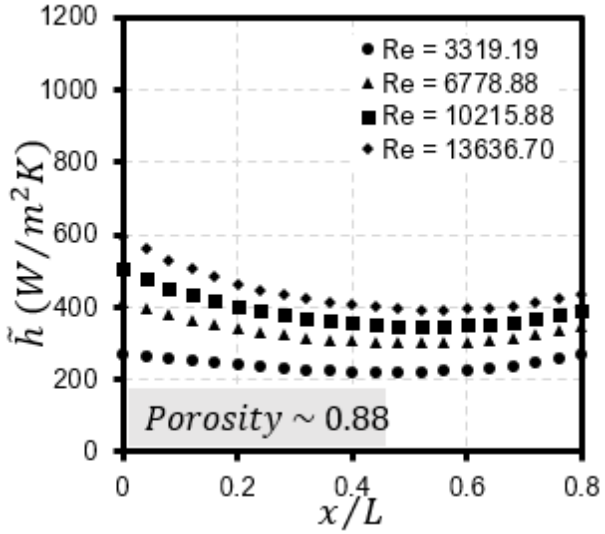

Fig. 19 Local convective heat transfer coefficient variation with lattice porosity [S316 panel]

A similar trend was observed for SS316L panel (porosity- 0.8) (Fig. 19) where heat transfer coefficient levels dropped to lower levels, and this is attributed to the low solid phase thermal conductivity of SS316L compared to SS420.

Particle heat transfer experiments

Unlike air-based convection experiments, the particles which carry heat from the test section had to be transported back into the system. To this end, a bucket elevator-system was designed and developed. Buckets elevator works by rotating a set of a bucket attached to a chain or a belt, and by doing so, the buckets scoop the particles from the bottom of the elevator casing and discharge at the top. Bucket elevators are more complex to design and manufacture, compared to static screw elevator and drag chain conveyor. However, the benefits of their reliability, smaller footprint, and the ability to work at elevated temperatures outweigh the cost and complexity of the manufacturing process. The actual assembled test facility, assembly CAD model, instrumented heat transfer test

section, and schematic representation of heat transfer scenario involving falling particles are shown in Fig. 20. Particles are first stored at room temperature in the top hopper while the top and bottom walls of the sandwich panel was being electrically heated with patch heaters. The particles were held until the panel walls reach a temperature of 100ºC.

A gate valve was installed right downstream of the heat transfer section, which facilitated the on/off type flow of particle across the test section. Once the desired panel wall temperatures were achieved, the gate valve was flipped and the elevator was started at the same time, to allow the transport of the spent particle back into the top hopper via a series of equi-spaced buckets.

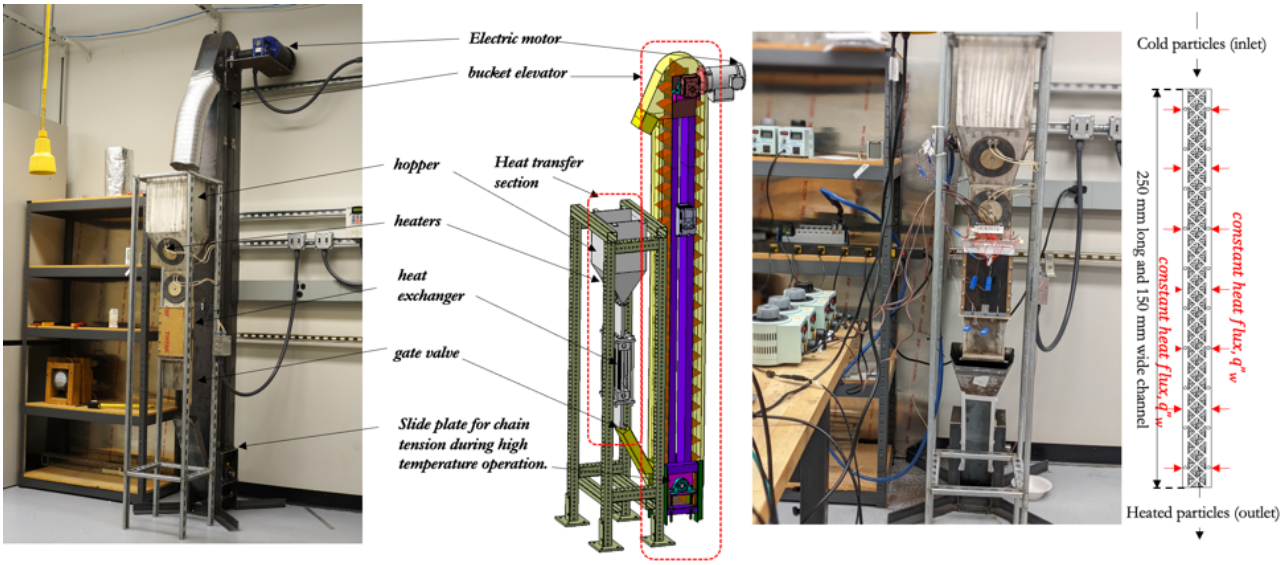

Fig.20 Particle heat transfer test facility

To this end, a novel quasi-steady state heat transfer methodology was devised exclusively for this part of the investigation, which could effectively provide local convective heat transfer coefficient where heat transfer was facilitated through falling particles. In this approach, firstly the hopper is filled with desired type of particles where the total mass of particles was decided such that a packed bed flow type could be achieved at the heat transfer test section. Once the hopper was charged with particles, the heating process was started where all the eight patch heaters occupying the entire 150 x 250 mm^2 panel on both left and right sides of sandwiched panel were heated. Once the steady-state heat transfer condition was obtained, the particle flow rate through the Octet panel was initiated by opening the gate valve installed at the bottom of the heat exchanger to 100%. Note that this facility also allows a fine control over the particle flow rate through the gate valve while still maintaining a packed moving bed through the Octet panel. In this study, the maximum possible particle mass flow rate was studied, hence 100% opening of the gate valve was set. Prior to the particle flow start, the data acquisition system was initiated which involved over 20 thermocouple measurements across the heat transfer test section, including a pair of temperature measurements for particle inlet and

outlet. Once the particles started to flow through the Octet panel, the walls of the panel started to cool down rapidly to a local minimum. At that point onwards, the particle and the wall temperatures continued to slowly increase through the rest of the transient experiment. In the heat transfer coefficient calculation, the wall and particle temperatures during this slow heat ramp up period was taken into consideration and the local convective heat transfer coefficient was determined through the following equation:

$$h(x,t) = \frac{q"_{conv}(t)}{T_w(x,t) - T_f(x,t)}$$

where, $q"_{conv}(t)$ is the heat convected away from the walls via the particles in motion and this was obtained by subtracting the local heat losses from the backside of the eight patch heaters occupying and supplying constant heat flux on the left and right sides of the panel. Note that the temperature drop across the insulation material was measured at multiple locations along the streamwise length and also recorded along with the wall temperature at the same frequency throughout the transient operation. The heat loss however was minimal compared to the total heat supplied.

Figure 21 shows the transient heat transfer measured at five locations in the streamwise direction for three types of particle flows through Octet panel of porosity 0.88 for both SS420 and SS316 panels. Only the highest porosity of panel was chosen since we wanted to study the particle diameter effect on the local heat transfer behavior of Octet panels and that the two lower porosities of the Octet panel (0.75 and 0.8) did not support unobstructred free flow of particles of all the diameters. For the smallest particle diameter (266 μm), the streamwise location closest to the hopper showed a fluctuating trend with a certain time period. The heat transfer levels at 5% of the streamwise length was nearly two times higher or more compared to the subsequent downstream measurement locations. Further, it is noted that the heat transfer coefficients are nearly constant over a period of 30 minutes which falls under the “quasi-steady” state regime of the transient experiment. For the intermediate particle diameter case (CP 30/60), the fluctuations in transient heat transfer coefficients were not observed and the time evolution of the same showed a nearly constant trend.

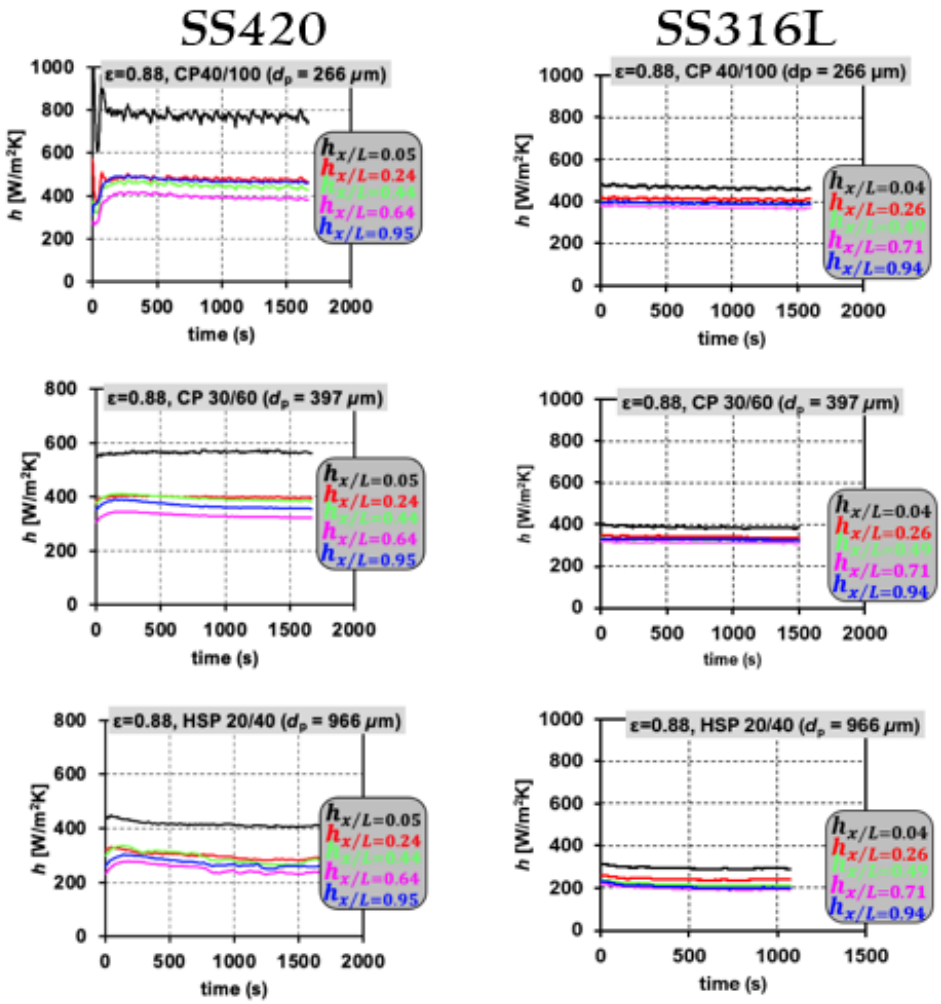

Fig. 21 Transient convective heat transfer coefficient at five different locations in the streamwise direction for three particle types (Octet panel porosity of 0.88) [SS420 panel (left), SS316L panel (right)]

The heat transfer rates were lower compared to the smallest particle diameter case (CP 40/100). This can be attributed to two factors: a) due to the smaller particle size, the particle flow speeds will be higher for CP 40/100 compared to CP 30/60, b) particle-to-particle, particle-to-gas, particle-to-fiber/endwall interactions will be more frequent for the smallest diameter case. The 2nd point should be further explore to Discrete Element Modeling (DEM) of particle flows through Octet lattices. For the largest diameter case (HSP 20/40), the heat transfer levels were further lower, thus supporting above two reasonings, while the temporal evolution exhibited some large time period fluctuations. However, the quasi-steady-state approach worked well for this particle case as well, as the heat transfer levels were nearly constant over the test duration.

Figure 22 shows the time-averaged convective heat transfer coefficient for particle flows through Octet lattice of 0,88 porosity. Figure 18 demonstrates that such a time-averaging is justified as the heat transfer coefficient was found to be time-independent in the quasi-steady state duration. A rapidly decreasing trend in heat transfer rates was

observed with increasing streamwise distance, which is a typical trend in developing thermal and fluid flow scenarios.

A near-periodic heat transfer regime was also observed at the 0.44 and 0.64 x/L locations, which can be considered as representative of the heat transfer coefficient to be expected for particle flows through long panels featuring Octet-shaped unit cells. A slightly increasing trend in heat transfer was observed towards the exit and this trend is attributed to the exit effects. The decrease in the heat transfer rates was only marginal in the x/L -> (0.44,64) regime for particle diameters 266 and 397 μm, however, a significant drop in heat transfer was observed for the largest particle diameter case.

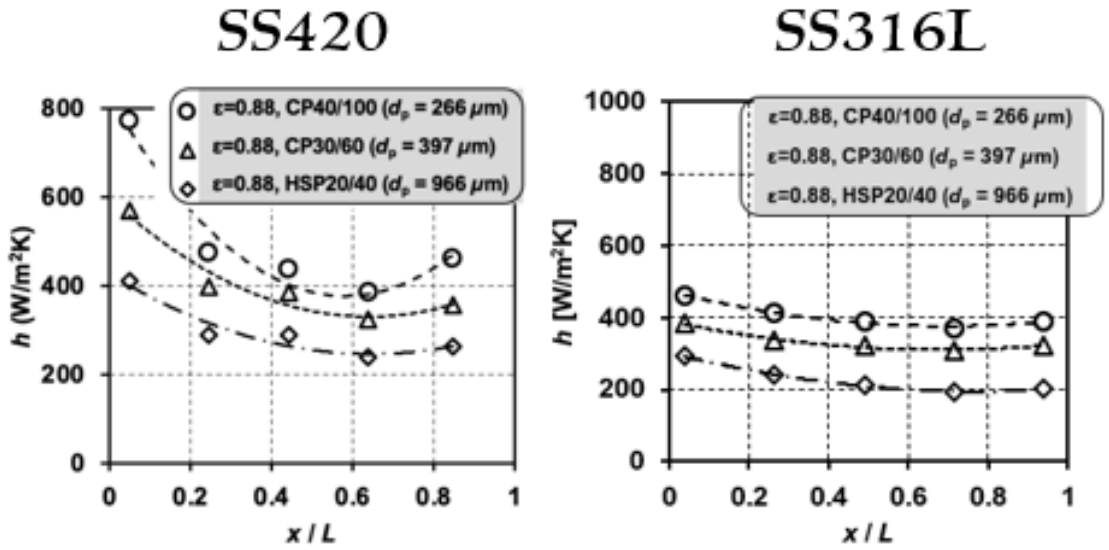

Fig. 22 Time-averaged convective heat transfer coefficient variation with streamwise location (Octet panel porosity of 0.88) [SS420 panel (left), SS316L panel (right)]

Particle-to-sCO2 heat exchanger design and development

The full calculation of the heat exchanger design and pressure drop was performed with a computer code using iterative approach. The code starts with an initial plate dimensions of 0.01mm and keep increasing the plate dimensions until the total stresses meet the required in ASME BPVC. After that, a CAD model of the plates was made according to the required dimensions and an assembly design of final heat exchanger is performed. Final dimensions and drawing of the heat exchanger core assembly is shown in the figure below.

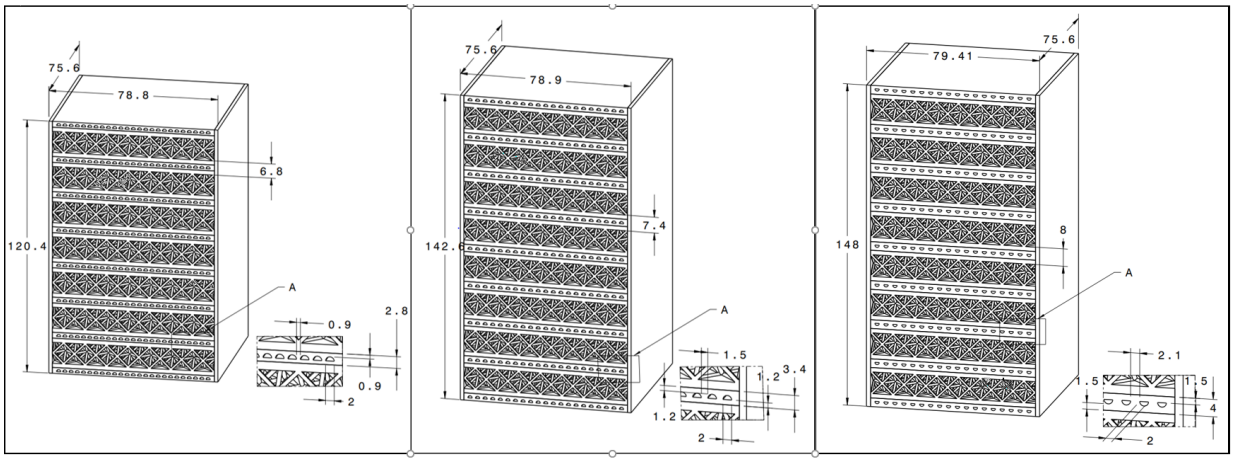

K = 1 *K = 2* *K = 3*

Figure 23: Heat exchanger assembly: (a) showing isometric view of the lattice hot side structure and plate containing sCO2 minichannels. (b) showing the top cut view of a single plate with minichannels configuration.

The octet panels are sandwiched between two plates containing sCO_2 minichannels. The 75.6 mm dimension for the octet panel is chosen due to the dimension limits required by the 3D printing company. The final heat exchanger design with extended plates for sCO_2 flow guidance and manifold are shown in the figure 24.

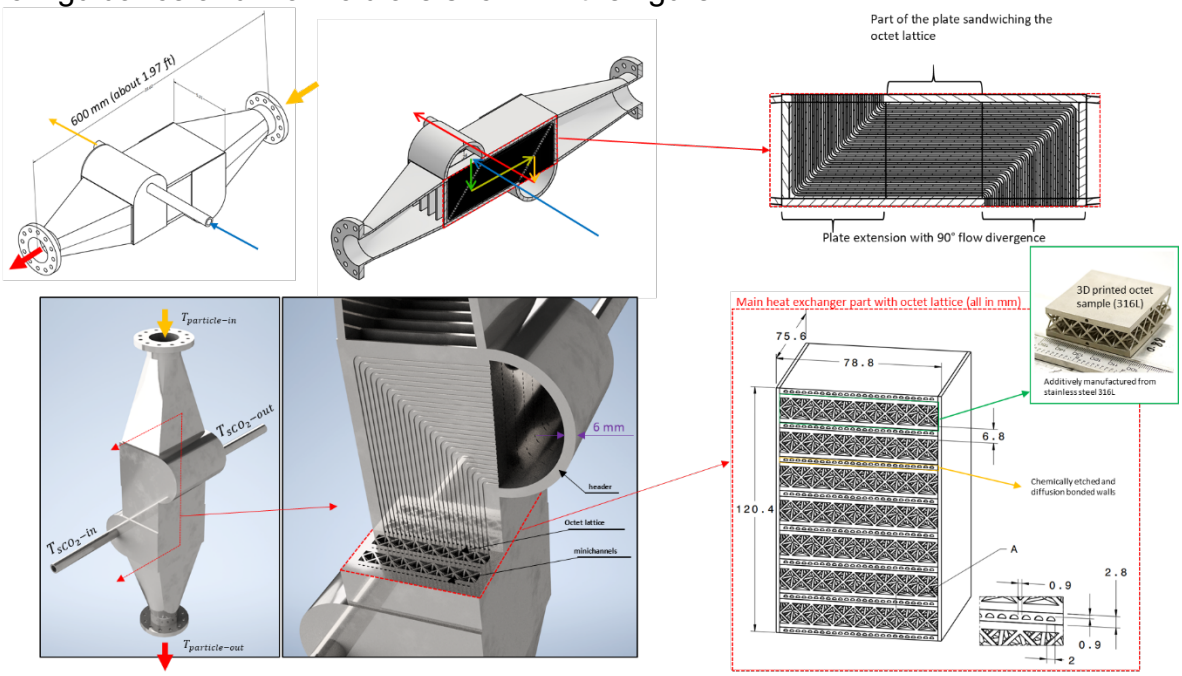

Figure 24: Heat exchanger design with manifold.

The assembled heat exchanger in the Sandia test bench is shown in Fig. 25, where the particle inlet/outlet and sCO2 inlet/outlet ports have been shown.

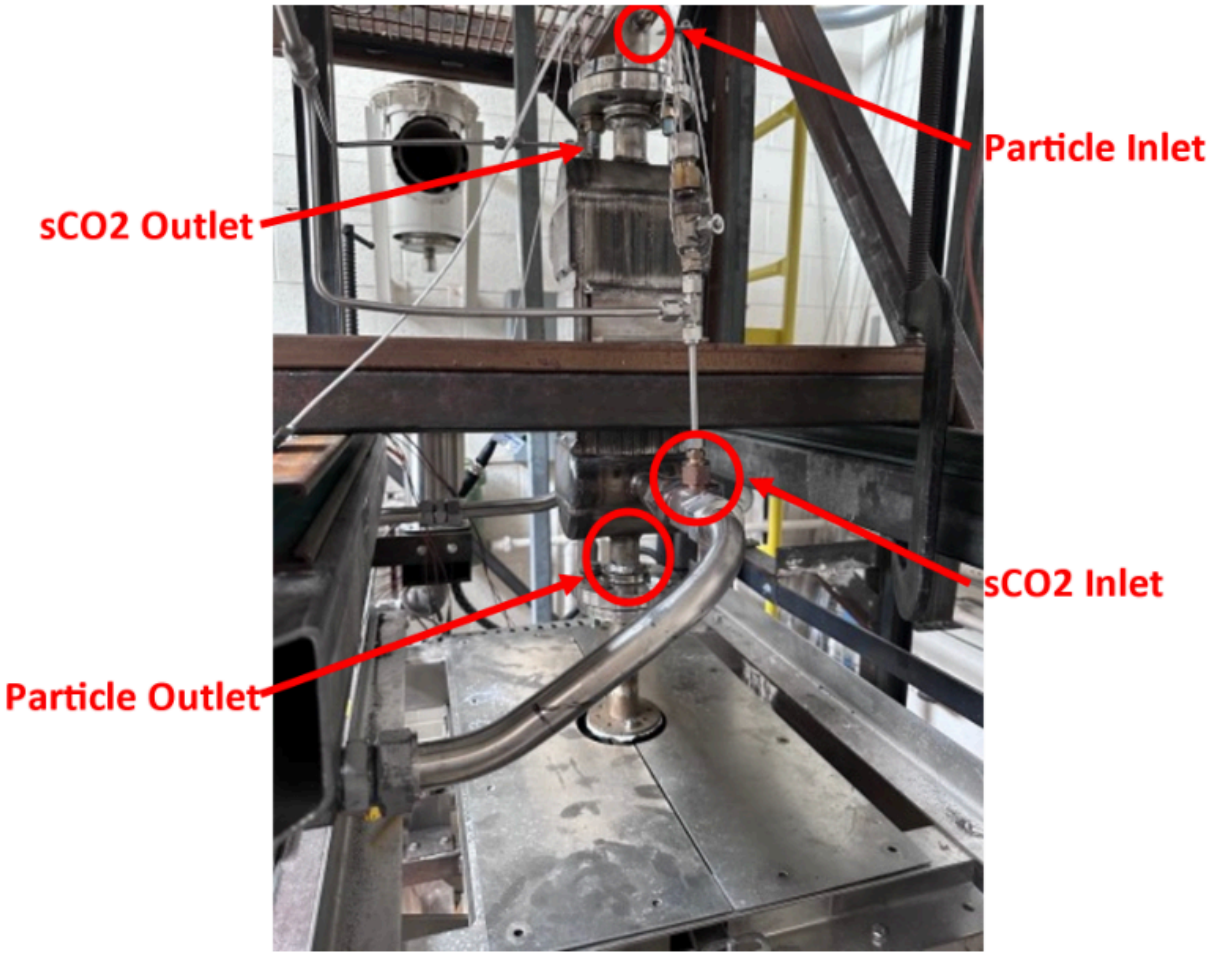

Figure 25: Assembly of particle-to-sCO2 HX at the Sandia test bench

Long duration tests were conducted at the Sandia test bench. Sandia's Heat Exchanger Test Stand facility is capable of testing experimental particle-to-sCO2 heat exchanger technology at the 20kW scale (Fig. 26). The facility provides the ability to conduct particle to sCO2 testing with prototype benchtop scale equipment. The system contains a 60kW particle-side capable of storing, heating, and circulating 500lbs of ceramic particle material continuously. The system also contains a 20kW sCO2 system capable of compressing CO2 gas to super critical conditions and delivering it to test equipment at up to 250 grams/second. Recirculation loops, recuperators, heaters, Coriolis flow meters, chillers, relief valves, and a custom-built control system allow fine control of flow rate, density, and temperature up to 2600 psig and 550 °C.

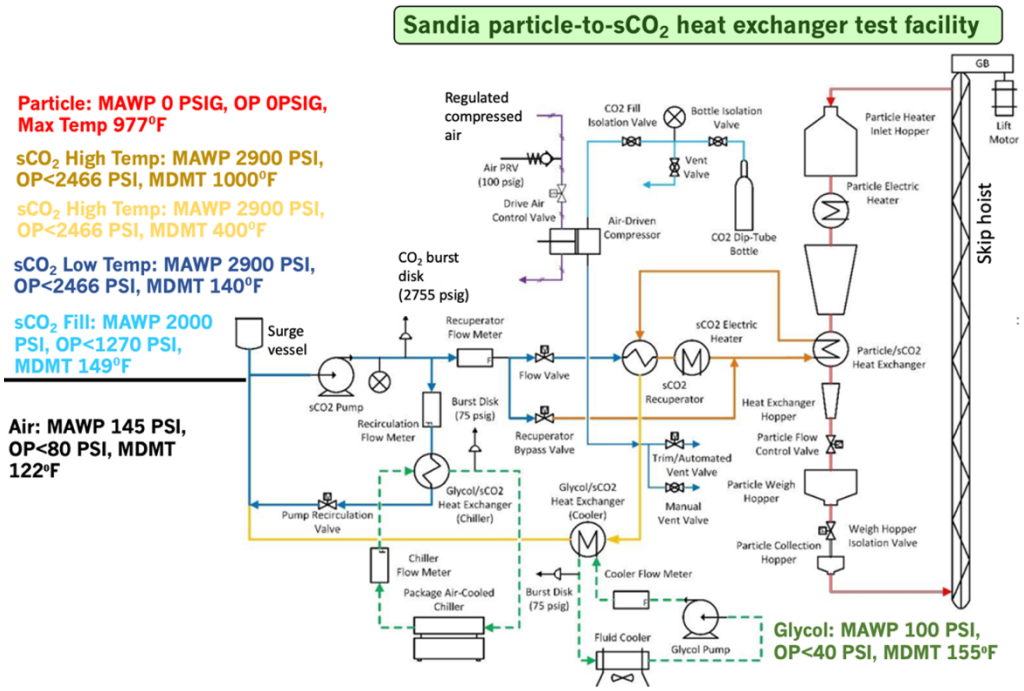

Figure 26: Schematic of Sandia test facility

Figure 27 shows the transient run conducted at the Sandia test bench at a fixed particle mass flow rate, while the sCO2 flow rates were varied at three different levels. The variation of sCO2 mass flow rates can be seen in the temperatures of the sCO2 at the outlet of the heat exchanger.

For the case when particle mass flow rate was three times that of sCO2, a temperature increase of 140 degree Celsius was observed in sCO2 line for 50 degree C drop in particle temperature.

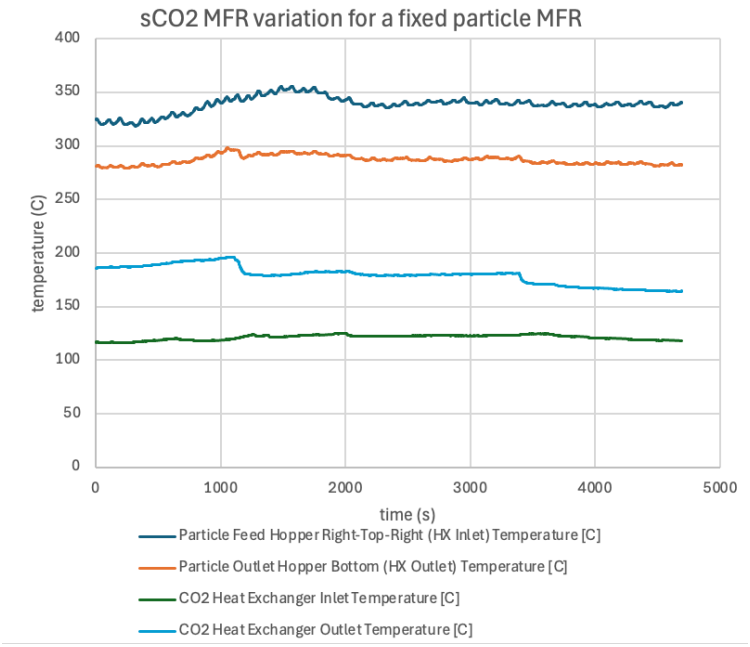

Figure 27: Temperature variation of particle and sCO2 for a fixed particle MFR while sCO2 MFR operated at three different levels

Parametric study for overall heat transfer coefficient (U) and total heat transfer (Q) with input h_{sw} (ξ) profiles for MPBHX with Octet metal foams

A parametric study was conducted and the detailed results are presented here to show the effects of the solid mass flow rate ($\dot{m}_{s,in}$), sCO_2 mass flow rate ($\dot{m}_{g,in}$), the sCO_2 channel width (W_g), and the inlet solid ($T_{s,in}$) and sCO_2 temperatures ($T_{g,in}$) on the U and Q of the MPBHX in presence of the Octet metal foams. The effect of width of the gas channel on the U and Q is shown in Figs. 28(a, b). It is observed that the U and Q values decrease as W_g increases, for the same mass flow rate when W_g increases it decreases the sCO_2 velocity through the channel. The decrease in sCO_2 velocity causes a decrease in the heat transfer coefficient from the sCO_2 to wall and hence U as well as Q decrease.

The effect of $\dot{m}_{s,in}$ on the total heat transfer (Q) is shown in Fig. 29. It is observed that Q increases with an increase in $\dot{m}_{s,in}$ and appears to converge to a value with further increase in $\dot{m}_{s,in}$. The increase in the solid mass flow rate increases the energy input into the HX which is provided by the hot solid bed. The Q appears to converge to a value as the HX is approaching the maximum heat transfer it can facilitate for the current HX area and sCO_2 flow configuration. The effect of $\dot{m}_{g,in}$ on the U and Q is shown in Figs. 30 (a,b) respectively. Both U and Q increase with an increase in $\dot{m}_{g,in}$, as the increase in the gas flow rate increases the gas velocity, leading to an increases in the wall-sCO_2 heat transfer coefficient, the overall increase in U, as well as the total heat transfer Q.

Finally, the effects of the solid-bed inlet temperature and sCO_2 inlet temperature on the total heat transfer are shown in Figs. 31 (a,b) respectively. In Fig. 31(a) the increase in Q due to an increase in $T_{s,in}$ is caused by the higher temperature of inlet solid particles, which increase the energy input into the HX, whereas for the sCO_2 inlet temperature the Q decreases as the inlet temperature increases. Due to the presence of Octet metal foam fibers, the HX can extract a higher amount of heat from the solid bed and transfer it into the sCO_2 stream. So, the sCO_2 with lower inlet temperature can absorb a higher amount of Q.

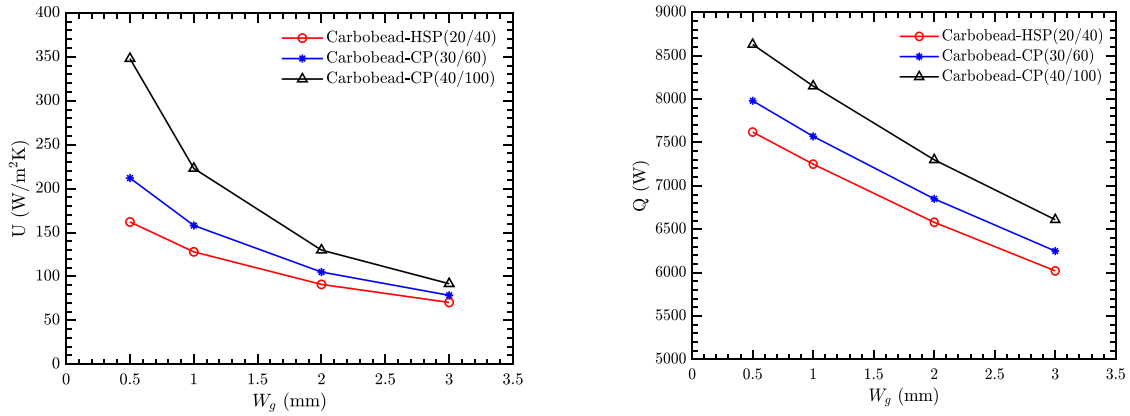

(a) **(b)**

Fig. 28 Variation of (a) overall heat transfer coefficient (U) and (b) total heat transfer (Q) with variation in sCO_2 channel width (W_g).

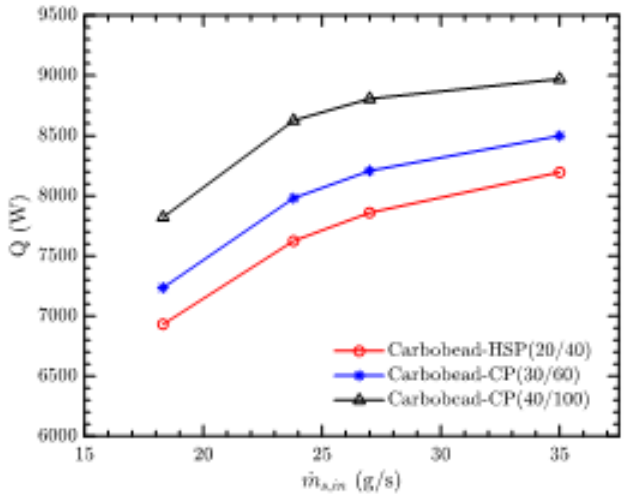

Fig. 29 variation of total heat transfer with particle mass flow rate

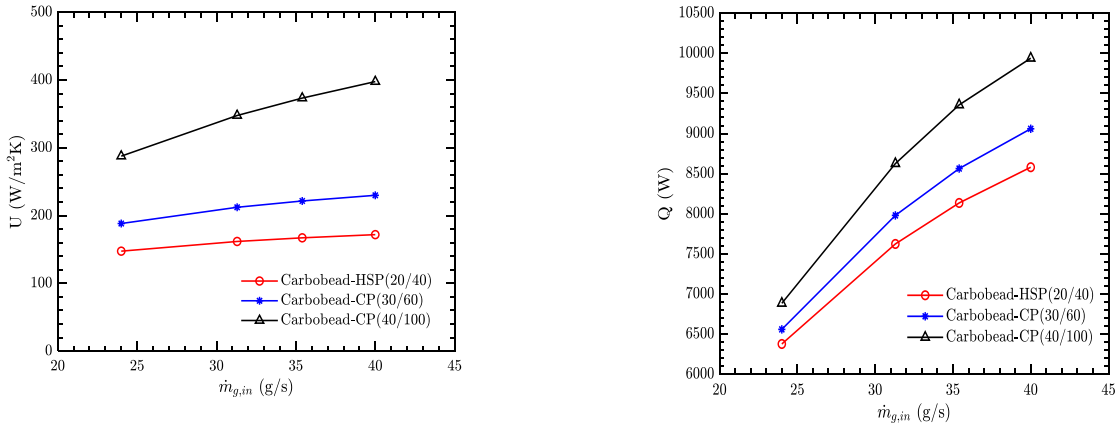

(a) **(b)**

Fig. 30. Variation of (a) overall heat transfer coefficient (U) and (b) total heat transfer (Q) with sCO_2 mass flow rate ($\dot{m}_{g,in}$).

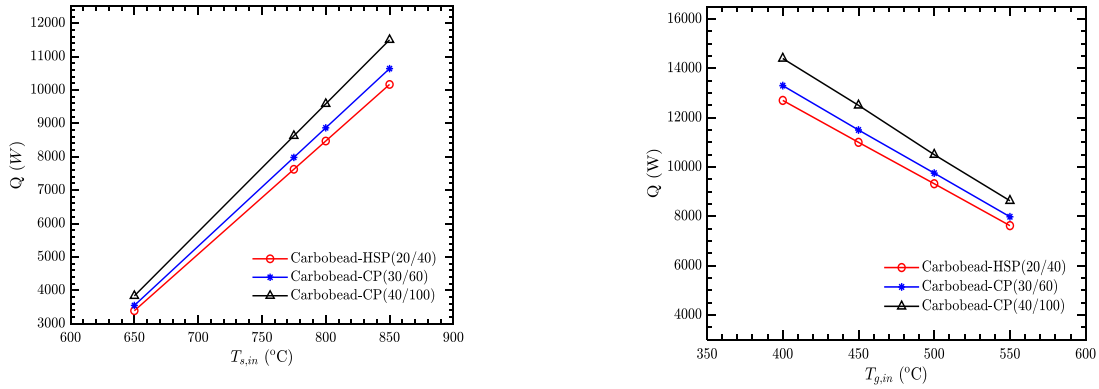

(a) **(b)**

Fig. 31. Variations of total heat transfer (Q) with (a) solid inlet temperature ($T_{s,in}$) and (b) sCO_2 inlet temperature ($T_{g,in}$).

Discrete element modeling of granular flow of particles through Octet lattice

In addition, we also conducted a comprehensive investigation to understand the fundamental flow and thermal transport of particles through Octet lattice. DEM simulations were conducted using LIGGGHTS software. Figure 32 shows the experimental setup along with the computational domain, which included a hopper which fed the lattice channel. Experiments were conducted with three different CARBOBEAD particles with their particle diameters ranging between ~250-1000 microns. Figure 33 shows the experimentally obtained snapshots of granular flow of particles for different particle sizes. Figure 34 shows the detailed particle-level flow predictions obtained through DEM.

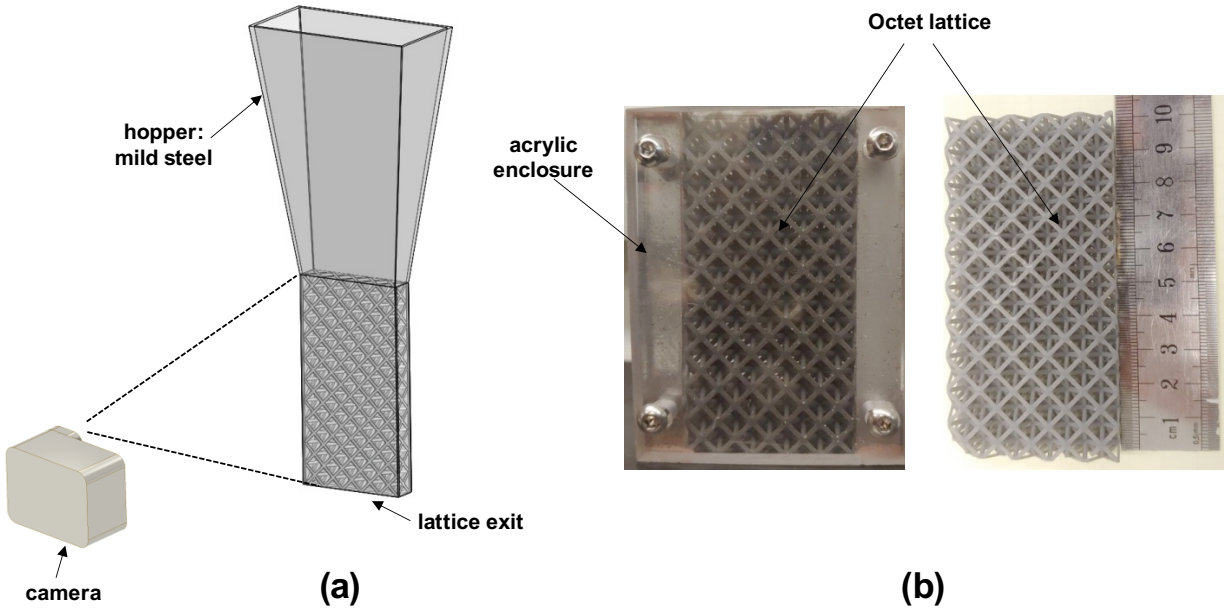

Fig. 32 Schematic of experimental set-up used for granular flow visualization (not drawn to scale), (b) additively manufactured Octet lattice packed between enclosure of acrylic glass

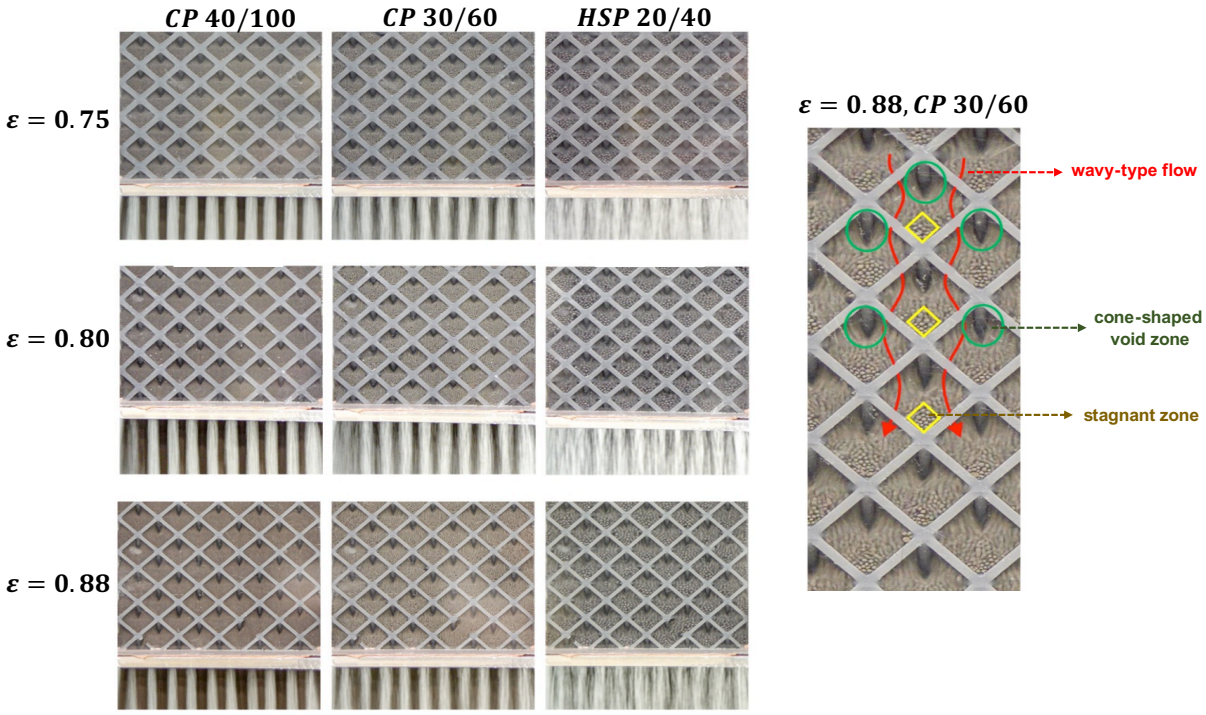

Fig. 33 Instantaneous images of the free-fall of particles in three different lattices taken during experiments

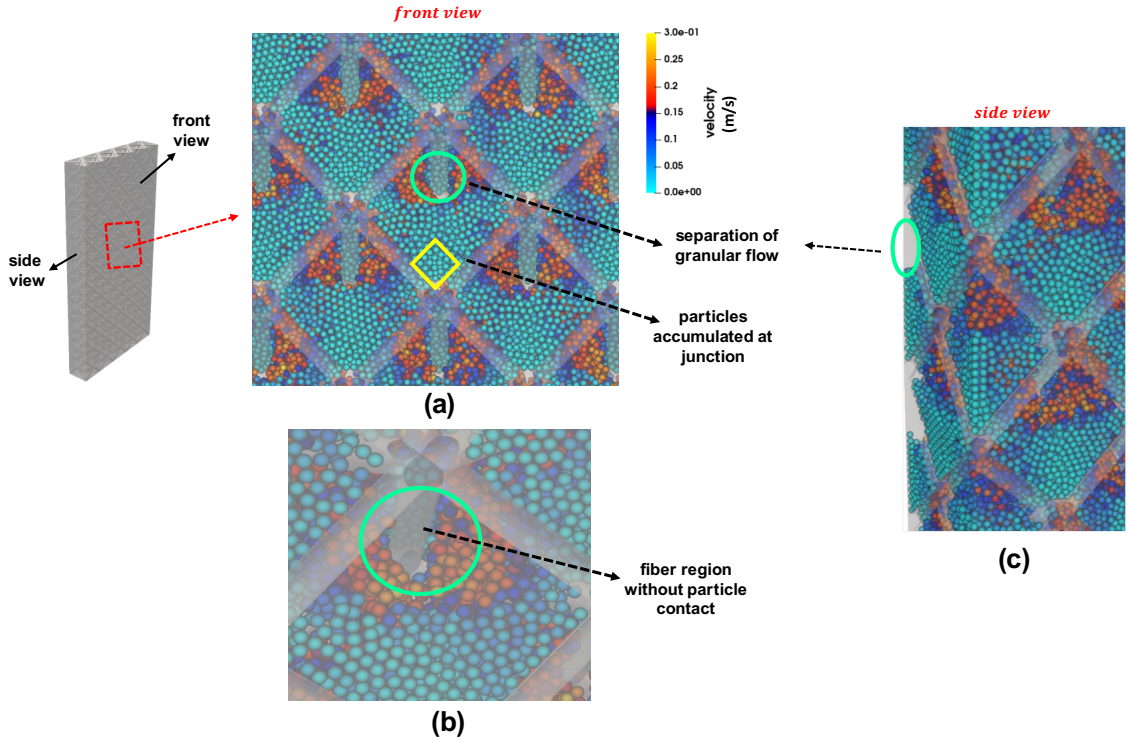

Fig. 34 Instantaneous image of the free-fall of particles from DEM simulations with particles colored with their local flow velocities, (b) zoomed-in view of the front side of the channel, and (c) zoomed-in side view of the channel

From the front view, three distinct flow characteristics were observed, i.e., (a) stagnant-zone upstream of the fiber junctions, (b) cone-shaped void zone in the wake of the fibers, and (c) unobstructed wavy-type motion of particles on lateral sides of the fibers. The upstream stagnation of particles and downstream void due to particle separation is a common characteristic of granular flow around tubes in a shell-and-tube type heat exchanger. The downstream regions of fibers typically remain devoid of the contact with the heated particles leading to weaker heat transfer. The overall conjugate heat transfer coefficient of OLHX depends on the effective thermal conductivity of the system and interfacial heat transfer coefficient values. The interfacial heat transfer coefficient depends on the flow fields rendered by the moving media in the lattice. The local heat transfer coefficient distribution around discrete arrangement of circular tubes arranged normally and inclined to the mean flow direction is reported in literature. However, the current OLHX represents a relatively complex scenario where all the cylindrical fibers of the repeating unit cell are placed at a different angle to the encountering particles. The solid fibers attached to the bounding walls when fabricated in metal will develop thermal gradients internally leading to interesting thermal exchange dynamics with the particles.

8. **Significant Accomplishments and Conclusions**: In this project, we successfully demonstrated the benefits of metal additive manufacturing in realizing highly complicated structures which could result in significant performance enhancement in thermal transport from particles. We also demonstrated that AM-based coupons can be integrated with diffusion-bonded channels to result in a large-scale heat exchanger for high temperature application, where the cold side was at high pressure while the hot side was at ambient pressure and high temperature. High temperature/high pressure applications are challenging as they pose significant material-related challenges. Through this project, we overcame those challenges and also demonstrated significant performance enhancements in heat exchanger performance.

9. **Path Forward:** The path forward is to investigate new high temperature materials from the context of additive manufacturing, diffusion bonding, brazing and welding. The manufacturing efforts should also focus on joining dissimilar materials together to expand the design domain and to achieve high performance at high pressure/high temperature conditions. Detailed long duration experiments need to be conducted to characterize the flow and thermal transport behavior of particles when they move through complex pathways. The long-term effects of material wear and degradation when subjected to particle flows in moving packed bed formation needs to be understood through a combination of experimental and computational approach.

10. **Products:**

- Aider, Y., Cho, H. and Singh, P., 2022, July. Convective Heat Transfer Potential of Particles/Airflow Through Single Cell Thick Additively Manufactured Octet-Shaped Lattice Frame Material. In Heat Transfer Summer Conference (Vol. 85796, p. V001T06A004). American Society of Mechanical Engineers.

- Kaur, I., Aider, Y., Cho, H. and Singh, P., 2024. Granular Flow in Novel Octet Shape–Based Lattice Frame Material. Journal of Solar Energy Engineering, 146(3).

- Aider, Y., Kaur, I., Mishra, A., Li, L., Cho, H., Martinek, J., Ma, Z. and Singh, P., 2023. Heat transfer characteristics of particle and air flow through additively manufactured lattice frame material based on octet-shape topology. Journal of Solar Energy Engineering, 145(6), p.061004.

- Aider, Y., Mishra, A., Li, L., Cho, H. and Singh, P., 2022, October. Heat Transfer Characteristics of Particle Flow Through Additively Manufactured (SS 316L) Lattice Frame Material Based on Octet-Shape Topology. In ASME International Mechanical Engineering Congress and Exposition (Vol. 86700, p. V008T11A046). American Society of Mechanical Engineers.

- Mishra, A., Singh, P. and Li, L., 2024. Heat transfer model for moving packed-bed particle-to-sCO2 heat exchangers integrated with metal foams. Applied Thermal Engineering, 239, p.122062.

- Mishra, A., Korba, D., Kaur, I., Singh, P. and Li, L., 2023. Prediction and Validation of Flow Properties in Porous Lattice Structures. Journal of Fluids Engineering, 145(4), p.041402.

11. Project Team and Roles:

Name: Prof. Prashant Singh
Affiliation at the time of award receipt: Mississippi State University
Current affiliation: University of Tennessee, Knoxville
Project role: Principal Investigator / Prime recipient
Contributions: Project management and supervision of research, data collection, reporting, presentations to DOE program manager.

Name: Prof. Like Li
Affiliation at the time of award receipt: Mississippi State University
Current affiliation: University of Central Florida
Project role: co-PI
Contributions: computational and analytical studies on particle flow through hot channel, technoeconomic analysis, overall heat exchanger effectiveness calculations.

Name: Prof. Heejin Cho
Affiliation at the time of award receipt: Mississippi State University
Current affiliation: University of Nevada, Las Vegas
Project role: co-PI
Contributions: Supporting heat transfer experiments with air/particles.

Name: Youssef Aider
Affiliation at the time of award receipt: Mississippi State University
Current affiliation: University of Tennessee, Knoxville
Project role: Graduate Research Assistant
Contributions: construction of experimental facilities for particle flow and thermal transport experiments, conducting heat transfer experiments with air/particles.

Name: Ashreet Mishra
Affiliation at the time of award receipt: Mississippi State University
Current affiliation: NA
Project role: Graduate Research Assistant
Contributions: computational and analytical studies on particle flow through hot channel, technoeconomic analysis, overall heat exchanger effectiveness calculations.

Name: Kevin Albrecht
Affiliation at the time of award receipt: Sandia National Laboratory
Current affiliation: NA
Project role: subrecipient

Contributions: communicating Sandia test bench specifications, help with design specifications of particle-to-sCO2 heat exchanger.

Name: Dimitri Madden
Affiliation at the time of award receipt: NA
Current affiliation: Sandia National Laboratory
Project role: subrecipient
Contributions: conducting experiments on the Sandia test bench, communicating results with the PI.

Name: Zhiwen Ma
Affiliation at the time of award receipt: National Renewable Energy Laboratory
Current affiliation: National Renewable Energy Laboratory
Project role: subrecipient
Contributions: technoeconomic analysis.

12. References:

[1] Renewables 2022 – Analysis, IEA (2022). https://www.iea.org/reports/renewables-2022 (accessed March 28, 2024).
[2] Solar, IEA (n.d.). https://www.iea.org/energy-system/renewables/solar-pv (accessed March 28, 2024).
[3] U.S. Solar Market Insight | SEIA, (n.d.). https://www.seia.org/us-solar-market-insight (accessed March 28, 2024).
[4] World Energy Outlook 2022 – Analysis, IEA (2022). https://www.iea.org/reports/world-energy-outlook-2022 (accessed March 28, 2024).
[5] Concentrating Solar Power Projects by Country | Concentrating Solar Power Projects | NREL, (n.d.). https://solarpaces.nrel.gov/by-country (accessed March 28, 2024).
[6] B. Zhao, M. Cheng, C. Liu, Z. Dai, System-level performance optimization of molten-salt packed-bed thermal energy storage for concentrating solar power, Applied Energy 226 (2018) 225–239. https://doi.org/10.1016/j.apenergy.2018.05.081.
[7] X. Wei, C. Yang, J. Lu, W. Wang, J. Ding, The mechanism of NO*x* emissions from binary molten nitrate salts contacting nickel base alloy in thermal energy storage process, Applied Energy 207 (2017) 265–273. https://doi.org/10.1016/j.apenergy.2017.06.109.
[8] S. Guccione, R. Guedez, Techno-economic optimization of molten salt based CSP plants through integration of supercritical CO2 cycles and hybridization with PV and electric heaters, Energy 283 (2023) 128528. https://doi.org/10.1016/j.energy.2023.128528.
[9] Q. Gong, A. Hanke, F. Kessel, A. Bonk, T. Bauer, W. Ding, Molten chloride salt technology for next-generation CSP plants: Selection of cold tank structural material utilizing corrosion control at 500 °C, Solar Energy Materials and Solar Cells 253 (2023) 112233. https://doi.org/10.1016/j.solmat.2023.112233.

[10] C.S. Turchi, S. Gage, J. Martinek, S. Jape, K. Armijo, J. Coventry, J. Pye, C.-A. Asselineau, F. Venn, W. Logie, A. Fontalvo, S. Wang, R. McNaughton, D. Potter, T. Steinberg, G. Will, CSP Gen3: Liquid-Phase Pathway to SunShot, National Renewable Energy Lab. (NREL), Golden, CO (United States); Sandia National Lab. (SNL-NM), Albuquerque, NM (United States); Australian National Univ., Canberra, ACT (Australia); Commonwealth Scientific and Industrial Research Organization (CSIRO), Newcastle, NSW (Australia); Queensland Univ. of Technology, Brisbane (Australia), 2021. https://doi.org/10.2172/1807668.
[11] W. Ding, T. Bauer, Progress in Research and Development of Molten Chloride Salt Technology for Next Generation Concentrated Solar Power Plants, Engineering 7 (2021) 334–347. https://doi.org/10.1016/j.eng.2020.06.027.
[12] M. Mehos, C. Turchi, J. Vidal, M. Wagner, Z. Ma, C. Ho, W. Kolb, C. Andraka, A. Kruizenga, Concentrating Solar Power Gen3 Demonstration Roadmap, 2017. https://doi.org/10.2172/1338899.
[13] C. Murphy, W. Cole, Y. Sun, M. Mehos, C. Turchi, G. Maclaurin, The Potential Role of Concentrating Solar Power within the Context of DOE's 2030 Solar Cost Targets, (2019). https://research-hub.nrel.gov/en/publications/the-potential-role-of-concentrating-solar-power-within-the-contex (accessed March 28, 2024).
[14] T.R. Mancini, J.A. Gary, G.J. Kolb, C.K. Ho, Power Tower Technology Roadmap and cost reduction plan., Sandia National Laboratories (SNL), Albuquerque, NM, and Livermore, CA (United States), 2011. https://doi.org/10.2172/1011644.
[15] M. Farchado, G. San Vicente, N. Barandica, F. Sutter, G. Alkan, D. Sánchez-Señorán, Ángel Morales, Performance improvement of CSP particle receivers by depositing spinel absorber coatings, Solar Energy Materials and Solar Cells 266 (2024) 112681. https://doi.org/10.1016/j.solmat.2023.112681.
[16] K.M. Chung, J. Zeng, S.R. Adapa, T. Feng, M.V. Bagepalli, P.G. Loutzenhiser, K.J. Albrecht, C.K. Ho, R. Chen, Measurement and analysis of thermal conductivity of ceramic particle beds for solar thermal energy storage, Solar Energy Materials and Solar Cells 230 (2021) 111271. https://doi.org/10.1016/j.solmat.2021.111271.
[17] K.J. Albrecht, C.K. Ho, Design and operating considerations for a shell-and-plate, moving packed-bed, particle-to-sCO2 heat exchanger, Solar Energy 178 (2019) 331–340. https://doi.org/10.1016/j.solener.2018.11.065.
[18] C.K. Ho, M. Carlson, K.J. Albrecht, Z. Ma, S. Jeter, C.M. Nguyen, Evaluation of Alternative Designs for a High Temperature Particle-to-sCO2 Heat Exchanger, Journal of Solar Energy Engineering 141 (2019). https://doi.org/10.1115/1.4042225.
[19] J.A. Almendros-Ibáñez, A. Soria-Verdugo, U. Ruiz-Rivas, D. Santana, Solid conduction effects and design criteria in moving bed heat exchangers, Applied Thermal Engineering 31 (2011) 1200–1207. https://doi.org/10.1016/j.applthermaleng.2010.12.021.
[20] W. Fang, S. Chen, J. Xu, K. Zeng, Predicting heat transfer coefficient of a shell-and-plate, moving packed-bed particle-to-sCO2 heat exchanger for concentrating solar power, Energy 217 (2021) 119389. https://doi.org/10.1016/j.energy.2020.119389.

[21] P.A. Isaza, W.D. Warnica, M. Bussmann, Co-current parallel-plate moving bed heat exchanger: An analytical solution, International Journal of Heat and Mass Transfer 87 (2015) 616–624. https://doi.org/10.1016/j.ijheatmasstransfer.2015.02.079.
[22] P.A. Isaza, W.D. Warnica, M. Bussmann, Counter-current parallel-plate moving bed heat exchanger: An analytical solution, International Journal of Heat and Mass Transfer 87 (2015) 625–635. https://doi.org/10.1016/j.ijheatmasstransfer.2015.02.056.
[23] J.-M. Yin, Q.-Y. Zheng, X.-R. Zhang, Heat transfer model of a particle energy storage-based moving packed bed heat exchanger, Energy Storage 2 (2020) e113. https://doi.org/10.1002/est2.113.
[24] J. Maskalunas, G. Nellis, M. Anderson, The heat transfer coefficient associated with a moving packed bed of silica particles flowing through parallel plates, Solar Energy 234 (2022) 294–303. https://doi.org/10.1016/j.solener.2022.01.052.
[25] S. Deng, Z. Wen, G. Lou, D. Zhang, F. Su, X. Liu, R. Dou, Process of particles flow across staggered tubes in moving bed, Chemical Engineering Science 217 (2020) 115507. https://doi.org/10.1016/j.ces.2020.115507.
[26] Y.L. Dai, X.J. Liu, D. Xia, Flow characteristics of three typical granular materials in near 2D moving beds, Powder Technology 373 (2020) 220–231. https://doi.org/10.1016/j.powtec.2020.06.057.
[27] P. Bartsch, S. Zunft, Granular flow around the horizontal tubes of a particle heat exchanger: DEM-simulation and experimental validation, Solar Energy 182 (2019) 48–56. https://doi.org/10.1016/j.solener.2019.01.086.
[28] X. Tian, J. Yang, Z. Guo, Q. Wang, B. Sunden, Numerical study of heat transfer in gravity-driven dense particle flow around a hexagonal tube, Powder Technology 367 (2020) 285–295. https://doi.org/10.1016/j.powtec.2020.04.001.
[29] X. Tian, F. Zhu, Z. Guo, J. Zhang, J. Yang, Q. Wang, Numerical investigation of gravity-driven particle flow along the trapezoidal corrugated plate for a moving packed bed heat exchanger, Powder Technology 405 (2022) 117526. https://doi.org/10.1016/j.powtec.2022.117526.